Article:
Garzón-Alvarado, D.A., Duque-Daza, C.A., Vaca-González, J.J. et al. (5 more authors) (2024) Part II: A new perspective for modeling the bone remodeling process: Biology, mechanics, and pathologies. Journal of Theoretical Biology, 593. 111894. ISSN 0022-5193

https://doi.org/10.1016/j.jtbi.2024.111894

Part II: A New Perspective for Modeling the Bone Remodeling Process: Biology, Mechanics, and Pathologies.

Diego A. Garzón-Alvarado[1,2,*], Carlos A. Duque-Daza[2], Juan Jairo Vaca-González[3], Abdelkader Boucetta[4], Dorian L. Linero[5], Gregory de Boer[6], Raj Das[7], and Salah Ramtani[4]

[1]*Biotechnology Institute, Universidad Nacional de Colombia, Colombia*
[2]*GNUM, Universidad Nacional de Colombia, Colombia*
[*]*Corresponding author: Diego A. Garzón-Alvarado, dagarzona@unal.edu.co*
[3]*Escuela de Pregrado - Direccion Académica, Universidad Nacional de Colombia*
[4]*Laboratoire CSPBAT, equipe LBPS, CNRS (UMR 7244),Universit e Sorbonne Paris Nord, France,* ramtani@univ-paris13.fr
[5]*Civil and Agricultural Department, Universidad Nacional de Colombia, Colombia ,* dllineros@unal.edu.co
[6]*School of Mechanical Engineering, University of Leeds, United Kingdom*
[7]*School of Engineering, RMIT University, Australia*

Abstract

In this paper, we explore the effects of biological (pathological) and mechanical damage on bone tissue within a benchmark model. Using the Finite Element Methodology, we analyze and numerically test the model's components, capabilities, and performance under physiologically and pathologically relevant conditions. Our findings demonstrate the model's effectiveness in simulating bone remodeling processes and self-repair mechanisms for micro-damage induced by biological internal conditions and mechanical external ones within bone tissue. This article is the second part of a series, where the first part presented the mathematical model and the biological and physical significance of the terms used in a simplified benchmark model. It explored the bone remodeling model's application, implementation, and results under physiological conditions.

***Keywords*—** Bone remodeling, Komarova's model, osteoclasts, osteoblasts, osteocytes

1 Introduction

This study introduces a novel framework for bone remodeling, emphasizing the interaction between mechanical and biological factors. In the proposed model, the boundary conditions and mechanical properties induced by external loads are considered, which promote the cellular activity of the BMU (comprising osteoblasts and osteoclasts) and the osteocytes. For this model, we will refer to this as the extended BMU (noting that osteocytes are not part of the BMU), i.e., ours integrates natural events like the Basic Multicellular Unit (BMU) (traditionally considered a system composed of osteoblasts and osteoclasts) alongside bone cells outside the BMU, such as osteocytes. However, recent articles have referenced the BMU as a cellular unit composed of osteoclasts, osteoblasts, and osteocytes (see [11]). This approach unifies biological processes with mechanical dynamics, producing a more realistic representation. By incorporating communication channels among bone cells, our model provides deeper insights into bone remodeling mechanisms. This new work sets the stage for further exploration in pathological and physiological contexts.

Previously, {Hambli [2014] introduced a {Finite Element model (FE model) that integrated cellular dynamics and mechanical behavior to simulate bone adaptation in response to external loadings. {The model accurately predicts human proximal femur adaptation patterns, revealing the intricate spatiotemporal dynamics of bone remodeling. It underscores the critical importance of the dynamic interplay between osteoclasts, osteoblasts, and mechanical stimuli. Also, the {Hambli et al., [2014] developed a computer model to simulate denosumab treatment effects on proximal femur bone remodeling, focusing on bone mineral density (BMD) changes. The model integrates pharmacokinetics and pharmacodynamics with a mechanobiological {FE model remodeling approach accounting for osteoclast and osteoblast activities. Mechanical behavior considers bone fatigue damage accumulation and mineralization, while a strain-damage stimulus function regulates bone cell factors [15]. By its part, {Bonfoh et al., [2011] used differential equations developed by Komarova et al., [2003], it describes how these factors respond to stimuli, affecting bone density. Near equilibrium, balanced activity occurs, while deviations

lead to bone apposition or resorption. Implemented in ABAQUS, the model analyzes bone structure response to mechanical loads, showing expected remodeling behavior [7]. In addition, Bahia et al., [2020] presented a mathematical model integrating bone cell activities and pharmacological dynamics for bone remodeling. It incorporates osteoblast-osteoclast signaling, mechanical stimuli, and drug effects. Simulations show the model's ability to capture bone's adaptive response, indicating the potential for therapy investigation and drug development for bone diseases [5]. In these works, it is common to emphasize understanding and modeling the complex interplay between bone cells, mechanical stimuli, and pharmacological effects in bone remodeling processes. They developed mathematical models that integrated various factors to predict bone adaptation patterns and responses to treatment. Additionally, they aim to provide insights into bone remodeling dynamics and potential therapeutic strategies for bone diseases.

{The studies by Ryser and colleagues [2010, 2009, 2012] collectively explore key aspects of bone remodeling and its implications in health and disease. Ryser et al., [2010] focuses on the mechanical properties of bone, elucidating how osteoclasts, osteoblasts, and osteocytes orchestrate bone remodeling through complex signaling involving RANKL and OPG within bone multicellular units (BMUs). Their mathematical model, employing nonlinear PDEs, predicts pathological remodeling scenarios and aligns computational results with in vivo observations, enhancing our understanding of spatial regulation in bone remodeling. Building on this, Ryser et al., [2009] investigate the spatio-temporal dynamics of BMUs, demonstrating how RANKL gradients influence osteoclast activity and subsequent osteoblast recruitment during bone resorption and formation cycles. This model underscores the critical role of local cellular interactions and gradients in maintaining bone structure and function. In a related context, Ryser et al., [2012] explores bone metastasis, where cancer cells manipulate osteoclasts via RANKL to enhance bone resorption for tumor expansion. They propose that tumor-produced OPG can locally modulate RANKL gradients, influencing osteolysis rates and tumor growth dynamics. Their mathematical framework highlights the importance of spatial distributions of RANKL, OPG, and tumor factors like PTHrP in understanding metastatic processes and suggests potential therapeutic targets for mitigating bone metastases. These studies collectively emphasize the intricate interplay of cellular dynamics and biochemical signaling in bone health, remodeling, and pathology, offering insights into therapeutic strategies for bone-related diseases, including cancer metastasis.

Other relevant works have studied the effect of bone remodeling and cancer diseases. For instance, in [1], it was studied the pronounced bone loss following secondary breast cancer and treatment, emphasizing the need for early intervention to mitigate these effects and preserve bone health in patients. The authors utilized the ABAQUS/UMAT software to simulate the behavior of bone tissue under the influence of breast cancer and its treatments. This approach allowed them to quantify the extent of bone loss, expressed as a decrease in bone volume fraction (BV/TV), and assess the impact of bone stimulation and the effectiveness of physical activity on recovery. For its part, Verbruggen and McNamara [2023] quantified mechanical environment changes during bone metastasis using FEA models from μCT images of metastatic mouse bone. Time-dependent mechanical stimuli alterations near tumor masses were investigated for potential osteolysis cues. In the same direction, analyzing cancer, Baldonedo et al., [2020] introduced a bone remodeling model for myeloma disease, represented by a coupled nonlinear system of parabolic partial differential equations. Numerical analysis, employing a hybrid implicit-explicit Euler scheme within the {FE model, is conducted to approximate the solution. Although long bones have been widely studied, there are some studies in flat bones; for instance, Yang et al., [2022] explored skull remodeling strategies to enhance tumor treating fields (TTFields) therapy for glioblastoma (GBM). Using a {FE model, various techniques such as skull thinning, drilling, and cranioplasty with different materials are modeled. Results indicate that skull thinning and drilling increase TTFields intensity, with the number and area of burr holes correlating with enhancement. These investigations have shown advanced computational techniques, such as {FE model and mathematical modeling, to quantify mechanical changes during bone metastasis and explore innovative strategies for enhancing treatment efficacy in cancer patients.

{Based on the literature mentioned above, it can be observed that, to the author's best knowledge, no model includes both biological and mechanical damage simultaneously. While there are significant articles on the spatiotemporal distribution of bone cells during the remodeling process [6, 14, 15, 26–28, 36], this article explores how cells play a crucial role in damage removal and continuous structural adaptation to support external loads in a benchmark model. Additionally, unlike previous important articles, the model allows for mechanical, cellular, and biological damage, including diseases like tumors. The work developed here has been numerically compared and validated with previously conducted and published models in the literature [13, 32, 33]. In these models, a tree-like structure formation is demonstrated, emulating the formation of trabecular structures in bone but within a simplified geometry, such as the square presented here. Since we are exploring the mathematical model, its strengths, and weaknesses, the model is a "toy" to demonstrate that it can predict observable patterns in other models. It can also be extended to more complex models, i.e., coupled mechanical and biological damage models. Therefore, this article aims to validate a model previously presented in Part I of this series of articles, test its robustness against different types of damage, and how it can be regenerated (reduced) over time through bone turnover due to bone remodeling. However, the model also demonstrates how, beyond recoverable damage, there may be instances of abnormal bone apposition or reduction in bone mass. This article is the second part of a series. In the first part, we introduced the mathematical model, detailing the biological and physical significance of the terms used within a simplified benchmark model. We thoroughly explored the application, implementation, and outcomes of the bone remodeling model under physiological conditions. This initial study provided a foundational

understanding of the model's capabilities and limitations in simulating natural bone remodeling. In this second part, we build upon that foundation by delving deeper into the model's applicability to more complex scenarios. We extend our investigation to include mechanical and biological damage, exploring how the model can simulate the bone's response to various pathological conditions, such as tumors. By expanding the scope of our study, we aim to demonstrate the robustness and versatility of the model in predicting bone remodeling dynamics under different types of stress and damage. Thus, this work could serve as the initial conceptual framework for a general model of bone behavior during remodeling and in response to pathological internal agents or external mechanical factors.

2 Bone remodelling process: In brief

{This article is the second part of a series. In the first part, we introduced a comprehensive mathematical model for bone remodeling, explaining the biological and physical significance of the various terms used. The model was presented in a simplified benchmark form, allowing for an in-depth exploration of its utilization, implementation, and results under physiological conditions. Specifically, we demonstrated how the model accounts for the interactions between osteoclasts, osteoblasts, and osteocytes and contributes to the bone remodeling process. These interactions, in turn, interact with the deposited bone mass to remove and add bone tissue and to repair damage induced by daily bone usage. The entire model was detailed in the first part of this series, and we recommend readers review that work for a thorough understanding. Nevertheless, the model is briefly presented again here, as outlined below, to provide context and continuity. See 1.

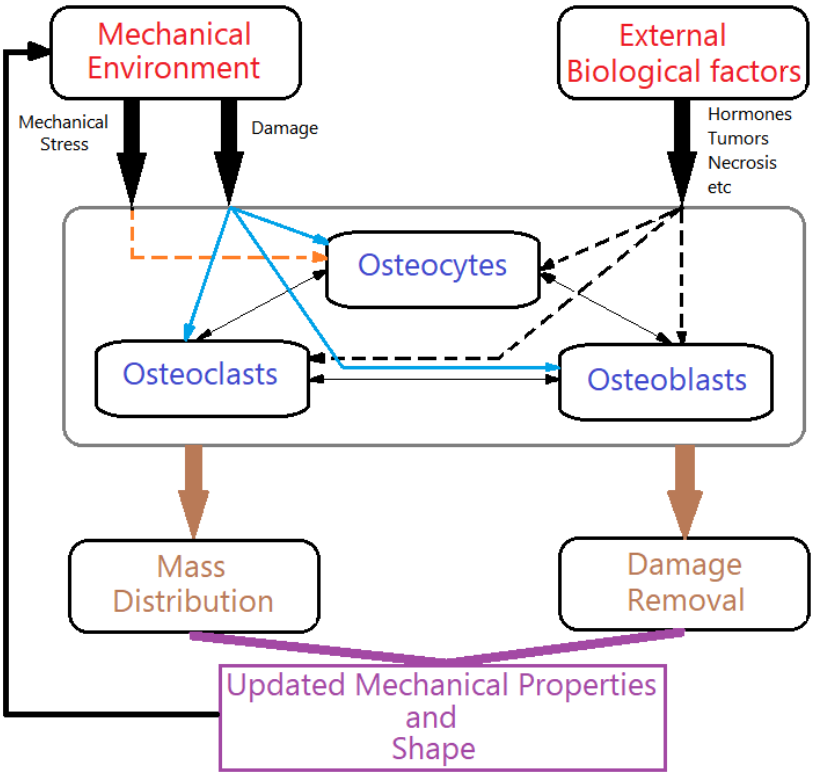

Figure 1: {Biological and mechanical factors stimulate bone remodeling. The figure shows the interaction between osteocytes, osteoclasts, and osteoblasts (arrows in blue). It illustrates how cellular communication and the external mechanical environment, including induced damage and mechanical stress, as well as external biological agents (arrows in black) (such as tumors, necrosis, hormones, etc.), affect the cells within the bone, especially, the mechanical environment affects the osteocytes (arrows in orange). The bone can improve its mass distribution through cellular self-regulation and remove damage caused by daily mechanical loads and induced biological defects (arrows in gold). This process allows for updating mechanical properties, affecting how the bone responds to mechanical stress (arrows in magenta).

The model starts with the static form of the force balance equation, also known as the momentum equation, is then given by [34]

$$\begin{cases} \nabla \cdot \sigma(\mathbf{x},t) + \mathbf{b} = \mathbf{0},\ \forall \mathbf{x} \in \Omega, & \text{(1a)} \\ \sigma(\mathbf{x},t) \cdot \mathbf{n}(\mathbf{x}) = \omega(\mathbf{x}),\ \forall \mathbf{x} \in \Gamma_N, & \text{(1b)} \\ \mathbf{u}(\mathbf{x}) = \mathbf{u_0}(\mathbf{x}),\ \forall \mathbf{x} \in \Gamma_D, & \text{(1c)} \end{cases}$$

In this context, $\sigma(\mathbf{x},t)$ denotes the Cauchy Stress tensor at time t, where $\mathbf{n}(\mathbf{x})$ signifies the outward-oriented unit vector, and $\mathbf{u_0}(\mathbf{x})$ represents the field of fixed displacement. {The other variables listed in the equation are $\mathbf{b}$, which is the body force per unit volume, in this case considered as $\mathbf{b} = 0$, and $\omega(\mathbf{x})$, which is the load per unit surface area. This corresponds to the load per unit length on the boundary in the two-dimensional case. The stress-strain constitutive relation for bone tissue, as elucidated in [13], is articulated as follows:

$$\sigma(\mathbf{x},t) = \mathbb{C}(\mathbf{x}, \mathbf{s}_{BMU}, \hat{D}(\mathbf{x},t,\hat{\beta}_1)) : \varepsilon(\mathbf{x},t), \tag{2}$$

where the strain tensor is given by $\varepsilon = \frac{1}{2}(\nabla \mathbf{u}(\mathbf{x},t) + \nabla \mathbf{u}(\mathbf{x},t)^T)$; {$\mathbf{s}_{BMU} = [s_0, s_1, s_2, z]^T$ is the extended BMU vector, where s_0, s_1, s_2, and z are the osteocytes, osteoclasts, osteoblasts, and bone mass, respectively; and $\hat{D}(\mathbf{x},t,\hat{\beta}_1)$ is the damage function which will be described below; hence the constitutive relationship is given by

$$\mathbb{C}(\mathbf{x}, \mathbf{s}_{BMU}, \hat{D}(\mathbf{x},t,\hat{\beta}_1)) = (\alpha_m \cdot (s_0(\mathbf{x},t))^{g_{0m}} \cdot (z(\mathbf{x},t))^{g_{zm}}) \cdot \mathbb{C}_0, \tag{3}$$

In Equation (3) α_m is a function that has into account the damage effect; {g_{0m} and g_{zm} are exponential factors that take into account the biological activity and maintain an equation structure similar to Komarova's model given by

$$\alpha_m = 1 - \hat{D}(\mathbf{x},t,\hat{\beta}_1), \tag{4}$$

In this framework, Osteocytes, alongside osteoclasts ($s_1(\mathbf{x},t)$) and osteoblasts ($s_2(\mathbf{x},t)$), regulate bone tissue dynamics at a given point $\mathbf{x}$. These cells collectively control the deposition and renewal of the bone matrix, measured as the percentage $z(\mathbf{x},t)$ within the vector $\mathbf{s}_{BMU} = [s_0, s_1, s_2, z]^T$. The term $g_{i,m}$ captures the joint impact of osteocytes (for $i = 0$) and bone mass percentage (for $i = z$) on the elasticity tensor governing mechanical properties. Mechanical damage, represented by $\hat{D}(\mathbf{x},t,\hat{\beta}_1)$, may arise from external factors like concentrated stress leading to fractures or accumulated stresses over time. Moreover, Damage accrues over time due to micro-damage within the tissue caused by mechanical stresses, as follows

$$D(\mathbf{x},t) = \sum_{\Delta t} \theta \sigma(\mathbf{x},t) \Delta t \tag{5}$$

Here, θ serves as a constant quantifying the damage induced by the stress $\sigma(\mathbf{x},t)$ over a specific time Δt. This damage persists until addressed during tissue remodeling, where osteoclasts resorb damaged tissue while osteoblasts generate new tissue at microdamage sites. Consequently, the damage is reset at the onset of each bone remodeling cycle. A sensor is designed to detect temporal changes in tissue density. It is derived from the bone mass percentage function z, using a subset of temporal points (r points) and employing linear regression $\hat{z} = \hat{\beta}_0 + \hat{\beta}_1 t$. This sensor accounts for variations in slope during remodeling. The sensor's expression is:

$$\hat{\beta}_1 = \frac{\sum_{i=1}^{r} (z_i t_i) - r\bar{z}\bar{t}}{\sum_{i=1}^{r} (z_i)^2 - \frac{1}{r}\left(\sum_{i=1}^{r} z_i\right)^2} \tag{6}$$

Here, t_i and z_i represent the time and bone mass percentage for the i-th point in the interpolation. $\bar{z}$ and $\bar{t}$ denote the averages of the points for z and t, calculated as $\bar{z} = \frac{1}{r}\sum_{i=1}^{r} z_i$ and $\bar{t} = \frac{1}{r}\sum_{i=1}^{r} t_i$. {The value of $\hat{\beta}_1$ is extensively explained in Part I of this series of articles. However, it is important to note that this parameter measures the slope of the bone mass curve (with respect to time), which fluctuates during the bone remodeling cycle at a material point. When the slope is positive or zero, it indicates that bone mass is being deposited and the bone tissue is being renewed. During this phase, damage due to external loads is also accumulating. Conversely, when the slope is negative, the bone is undergoing resorption, replacing the damaged tissue and starting the process anew with no damage (due to the replacement).. Consequently, the damage function is finalized by

$$\hat{D}(\mathbf{x},t,\hat{\beta}_1) = \begin{cases} 0 & \text{if } \hat{\beta}_1 < 0 \\ D(\mathbf{x},t) & \text{if } \hat{\beta}_1 \geq 0 \end{cases} \tag{7}$$

Utilizing equation 7 allows identifying tissue replacement instances and tracking microdamage accumulation over time. Osteocytes perceive mechanical stress as energy ($U = \frac{1}{2}\sigma : \varepsilon$) and interact with osteoblasts and osteoclasts to enhance bone's mechanical properties. As detailed in subsequent sections, damage can also result from abnormal metabolic conditions. Thus, bone mass progression is computed over time at each material point to assess damage extent based on biological and mechanical conditions.

From a biological standpoint, the bone remodeling process is governed by four interconnected nonlinear differential equations described by the state vector $\mathbf{s}_{BMU} = [s_0, s_1, s_2, z]^T(\mathbf{x},t)$ at material point $\mathbf{x}$ and time t. It is essential to remark osteocytes are not considered part of the BMU but to reduce jargon and simplify the notation, we are going to include it in the vector before mentioned, such as:

$$\begin{cases} \dfrac{ds_0}{dt} = \alpha_0 s_0^{g_{00}} s_1^{g_{10}} s_2^{g_{20}} - \beta_0 s_0 & (8a) \\ \dfrac{ds_1}{dt} = C_{BMU}\alpha_1 s_0^{g_{01}} s_1^{g_{11}} s_2^{g_{21}} - \beta_1 s_1 & (8b) \\ \dfrac{ds_2}{dt} = C_{BMU}\alpha_2 s_0^{g_{02}} s_1^{g_{12}} s_2^{g_{22}} - \beta_2 s_2 & (8c) \\ \dfrac{dz}{dt} = k_0 y_0 - k_1 y_1 + k_2 y_2 & (8d) \end{cases}$$

where C_{BMU} is a coupling factor that considers the recruitment and integration as a unity of the BMU's cells through the master cell called osteocyte; {in addition, g_{ij} represents the influence of cell i on cell j through paracrine signaling, which can depend on the damage level or be simply constant factors. given by

$$C_{BMU} = \begin{cases} c & \text{if } \dfrac{U}{U_{ref}} s_0 > W \\ 0 & \text{Otherwise} \end{cases} \tag{9}$$

where c represents a constant that accounts for the level of integration and functioning of the Basic Multicellular Unit (BMU). For its part, osteocytes sense mechanical loading and utilize this information to communicate with osteoclasts, promoting bone resorption, and coordinate with osteoblasts to drive bone formation. {In addition, the parameter W refers to a dimensionless activation energy value of the BMU. This parameter allows for the comparison of the energetic activity (dimensionless) of the mechanical system per osteocyte $\left(\frac{U}{U_{\text{ref}}} s_0\right)$ at a material point. Therefore, this parameter becomes the threshold above which BMU cellular activity will exist and below which the BMU does not need to activate and its functioning is inhibited due to disuse. This value was determined through trial and error in this work.

Equation 8a outlines the temporal evolution of osteocytes, where the osteocyte count at a specific material point hinges on mechanical loading. This loading is gauged by comparing mechanical energy to a reference value, expressed as:

$$\alpha_0 = k \cdot f_D \cdot \frac{U}{U_{ref}}, \tag{10}$$

Here, k modulates osteocyte addition to the bone matrix based on mechanical loading, $\frac{U}{U_{ref}}$. Elevated ratios greater than 1 will produce osteocyte growth, while lower ones maintain cell count. f_D sets the survival and function thresholds for osteocytes within the BMU, expressed as:

$$f_D = \begin{cases} f & \text{if } \hat{D}(\mathbf{x}, t, \hat{\beta}_1) < d \\ 0 & \text{Otherwise} \end{cases} \tag{11}$$

where d is the limit of damage allowed before the BMU collapse and the factor β_0, is a parameter of the elimination rate of osteocytes, which gives

$$\beta_0 s_0 = k. \tag{12}$$

2.0.1 Osteoclasts/Osteoblasts

Equations 8b and 8c show the temporal evolution at a particular material point of the osteoclasts and osteoblasts. Those equations have Komarova's structure [19] with the coupling of osteocytes as master cells that control all the BMU activity. Following Ramtani el al. [23, 24], there are three main possibilities of including the biological damage (originated by tumors, bone diseases, metastasis, necrosis, among other options) named D_b. {It is important to remember that steady states are found by solving the equations when $\frac{ds_0}{dt} = 0$, $\frac{ds_1}{dt} = 0$, and $\frac{ds_2}{dt} = 0$ simultaneously. Therefore, the steady state can be determined. From there, initial conditions can be applied by making a small perturbation around the steady state (no greater than 10% in one of its variables) to produce oscillations similar to those observed in the bone remodeling process.

1- Through production and removal parameters

Using the production and removal parameters (α_i and β_i), the equations 13 become in

$$\begin{cases} \dfrac{ds_1}{dt} = C_{BMU}\widehat{\alpha_1(D_b)} s_0^{g_{01}} s_1^{g_{11}} s_2^{g_{21}} - \widehat{\beta_1(D_b)} s_1 & (13a) \\ \dfrac{ds_2}{dt} = C_{BMU}\widehat{\alpha_2(D_b)} s_0^{g_{02}} s_1^{g_{12}} s_2^{g_{22}} - \widehat{\beta_2(D_b)} s_2 & (13b) \end{cases}$$

The functions α_i and β_i in the equations are dependent on the biological damage (D_b). A detailed explanation of the selected parameters can be found in the work by Ramtani et al. [23, 24]. Table 1 presents the scenarios

proposed by Ramtani et al. [23, 24], providing a comprehensive overview of the model. It should be noted that the biological damage (D_b) ranges from 0 to 1 ($0 \leq D_b < 1$). Factors in the form of $\frac{(*)}{1-D_b}$ represent an increasing trend, whereas factors in the form of $(*)(1-D_b)$ indicate a decreasing trend. Scenario 0 in Table 1 represents the original Komarova model without biological damage. Conversely, the other scenarios demonstrate how the production or removal parameters are influenced by D_b, resulting in abnormal cellular behavior and an altered bone remodeling cycle. A comprehensive discussion on this topic can be found in [24]. Notably, the values of α_i and β_i in Table 1 are constants that can be determined using the stability analysis described by Ramtani et al. [23, 24] and Komarova et al. [19]. These parameters are complemented by the constants g_{ij} in this model.

Furthermore, the stability analysis enables the identification of the steady states for each model, as illustrated in Table 1.

Table 1: Details of production and removal parameters in terms of D_b [23, 24], and steady state solutions for each scenario, taken from [23, 24]. $\gamma = g_{12}g_{21} - (1-g_{11})(1-g_{22})$

Scenario	$\widehat{\alpha_1(D)}$	$\widehat{\alpha_2(D)}$	$\widehat{\beta_1(D)}$	$\widehat{\beta_2(D)}$	Associated steady states
0	α_1	α_2	β_1	β_2	$\bar{s}_1 = \left(\frac{\beta_1}{\alpha_1}\right)^{(1-g_{22})/\gamma}\left(\frac{\beta_2}{\alpha_2}\right)^{g_{21}/\gamma}$ $\bar{s}_2 = \left(\frac{\beta_1}{\alpha_1}\right)^{g_{12}/\gamma}\left(\frac{\beta_2}{\alpha_2}\right)^{(1-g_{11})/\gamma}$
1	$\frac{\alpha_1}{(1-D_b)}$	$\alpha_2(1-D_b)$	$\frac{\beta_1}{(1-D_b)}$	$\beta_2(1-D_b)$	
2	$\alpha_1(1-D_b)$	$\frac{\alpha_2}{(1-D_b)}$	$\beta_1(1-D_b)$	$\frac{\beta_2}{(1-D_b)}$	
3	$\frac{\alpha_1}{(1-D_b)}$	$\alpha_2(1-D_b)$	$\beta_1(1-D_b)$	$\frac{\beta_2}{(1-D_b)}$	$\bar{s}_1 = (1-D_b)^{\frac{2(1-g_{22}-g_{21})}{\gamma}}\left(\frac{\beta_1}{\alpha_1}\right)^{\frac{(1-g_{22})}{\gamma}}\left(\frac{\beta_2}{\alpha_2}\right)^{\frac{g_{21}}{\gamma}}$ $\bar{s}_2 = (1-D_b)^{\frac{2(-1+g_{11}+g_{12})}{\gamma}}\left(\frac{\beta_1}{\alpha_1}\right)^{\frac{g_{12}}{\gamma}}\left(\frac{\beta_2}{\alpha_2}\right)^{\frac{(1-g_{11})}{\gamma}}$
4	$\alpha_1(1-D_b)$	$\frac{\alpha_2}{(1-D_b)}$	$\frac{\beta_1}{(1-D_b)}$	$\beta_2(1-D_b)$	$\bar{s}_1 = (1-D_b)^{\frac{2(-1+g_{22}+g_{21})}{\gamma}}\left(\frac{\beta_1}{\alpha_1}\right)^{\frac{(1-g_{22})}{\gamma}}\left(\frac{\beta_2}{\alpha_2}\right)^{\frac{g_{21}}{\gamma}}$ $\bar{s}_2 = (1-D_b)^{\frac{2(1-g_{11}-g_{12})}{\gamma}}\left(\frac{\beta_1}{\alpha_1}\right)^{\frac{g_{12}}{\gamma}}\left(\frac{\beta_2}{\alpha_2}\right)^{\frac{(1-g_{11})}{\gamma}}$
5	$\frac{\alpha_1}{(1-D_b)}$	α_2	β_1	β_2	$\bar{s}_1 = (1-D_b)^{\frac{(1-g_{22})}{\gamma}}\left(\frac{\beta_1}{\alpha_1}\right)^{\frac{(1-g_{22})}{\gamma}}\left(\frac{\beta_2}{\alpha_2}\right)^{\frac{g_{21}}{\gamma}}$
6	α_1	α_2	$\beta_1(1-D_b)$	β_2	$\bar{s}_2 = (1-D_b)^{\frac{g_{12}}{\gamma}}\left(\frac{\beta_1}{\alpha_1}\right)^{\frac{g_{12}}{\gamma}}\left(\frac{\beta_2}{\alpha_2}\right)^{\frac{(1-g_{11})}{\gamma}}$
7	α_1	$\frac{\alpha_2}{(1-D_b)}$	β_1	β_2	$\bar{s}_1 = (1-D_b)^{\frac{g_{21}}{\gamma}}\left(\frac{\beta_1}{\alpha_1}\right)^{\frac{(1-g_{22})}{\gamma}}\left(\frac{\beta_2}{\alpha_2}\right)^{\frac{g_{21}}{\gamma}}$
8	α_1	α_2	β_1	$\beta_2(1-D_b)$	$\bar{s}_2 = (1-D_b)^{\frac{(1-g_{11})}{\gamma}}\left(\frac{\beta_1}{\alpha_1}\right)^{\frac{g_{12}}{\gamma}}\left(\frac{\beta_2}{\alpha_2}\right)^{\frac{(1-g_{11})}{\gamma}}$

2- Including the biological damage as a factor in the production term

Equations 8b and 8c have an extra factor considering the biological damage level. Also, the autocrine/paracrine parameters g_{d1} and g_{d2} correspond to the effect on osteoclasts and osteoblasts due to the biological damage which can come from tumors, necrotic regions, hormonal or metabolic abnormalities.

$$\begin{cases} \dfrac{ds_1}{dt} = C_{BMU}\alpha_1 s_0^{g_{01}} s_1^{g_{11}} s_2^{g_{21}} D_b^{g_{d1}} - \beta_1 s_1 & \text{(14a)} \\ \dfrac{ds_2}{dt} = C_{BMU}\alpha_2 s_0^{g_{02}} s_1^{g_{12}} s_2^{g_{22}} D_b^{g_{d2}} - \beta_2 s_2 & \text{(14b)} \end{cases}$$

where it can be noted that D_b has been included as a factor, resembling Komarova's structure. Using the equations 14, it is possible to find the steady state (employing the stability analysis considered in [23, 24]) given by:

$$\begin{cases} \bar{s}_1 = D_b^{(g_{d1}-g_{d1}g_{22}-g_{21}g_{d2})/\gamma}\left(\dfrac{\beta_1}{\alpha_1}\right)^{(1-g_{22})/\gamma}\left(\dfrac{\beta_2}{\alpha_2}\right)^{g_{21}/\gamma} & \text{(15a)} \\ \bar{s}_2 = D_b^{(g_{d2}g_{11}-g_{d1}g_{12}-g_{d2})/\gamma}\left(\dfrac{\beta_1}{\alpha_1}\right)^{g_{12}/\gamma}\left(\dfrac{\beta_2}{\alpha_2}\right)^{(1-g_{11})/\gamma} & \text{(15b)} \end{cases}$$

3- Including biological damage into the autocrine and paracrine factors

Ayati et al. [4] introduced a seminal work in which Komarova's equations [19] are modified in their autocrine/paracrine factors as follows:

$$\begin{cases} \dfrac{ds_1}{dt} = C_{BMU}\alpha_1 s_0^{g_{01}(D_b)} s_1^{g_{11}(D_b)} s_2^{g_{21}(D_b)} - \beta_1 s_1 & \text{(16a)} \\ \dfrac{ds_2}{dt} = C_{BMU}\alpha_2 s_0^{g_{02}(D_b)} s_1^{g_{12}(D_b)} s_2^{g_{22}(D_b)} - \beta_2 s_2 & \text{(16b)} \end{cases}$$

{where g_{ij} represents the influence of cell i on cell j through paracrine signaling. Each parameter g_{ij} now also depends on the existing biological damage in the bone. This is denoted as $g_{ij}(D_b)$, a new parameter (initially proposed by Ayati et al. [2010]) that, in turn, depends on the biological environment and its level of metabolic integrity. These exponents are given by $g_{11}(D_b) = g_{11}(1 + r_{11}D_b)$, $g_{21}(D_b) = g_{21}(1 + r_{21}D_b)$, $g_{12}(D_b) = g_{12}/(1 + r_{12}D_b)$, $g_{22}(D_b) = g_{22} - r_{22}D_b$, with r_{ij} as constants. In contrast with the previous models, it requires four new parameters compared to the original Komarova model. Originally, Ayati et al. [4] stated this model for tumors coupled with the bone remodeling process, i.e., the term $r_{ij}D_b$ produces the coupling between tumor and osteoclasts/osteoblasts interactions. Also, it is possible to obtain the steady state following the previous work [23], which is given by

$$\begin{cases} \bar{s}_1 = \left(\dfrac{\beta_1}{\alpha_1}\right)^{\frac{1-g_{22}+r_{22}}{\Lambda}}\left(\dfrac{\beta_2}{\alpha_2}\right)^{\frac{g_{21}(1+r_{21})}{\Lambda}} & \text{(17a)} \\ \bar{s}_2 = \left(\dfrac{\beta_1}{\alpha_1}\right)^{\frac{g_{12}}{\Lambda(1+r_{12})}}\left(\dfrac{\beta_2}{\alpha_2}\right)^{\frac{1-g_{11}(1+r_{11})}{\Lambda}} & \text{(17b)} \end{cases}$$

with $\Lambda = (g_{12}/(1+r_{12}))(g_{21}(1+r_{21})) - (1-g_{11}(1+r_{11}))(1-g_{22}+r_{22})$.

2.0.2 Bone mass

Equation 8d represents the bone mass percentage in the function of the osteocytes, osteoclasts, and osteoblasts. Each k_i is a constant that considers the effect of the cells (osteocytes $i = 0$, osteoclasts $i = 1$, and osteoblasts $i = 2$) on the bone mass. k_0 is the constant that takes into account the integration of the BMU in the bone mass construction, this integration is represented by y_0 as follows

$$y_0 = C_{BMU} - c, \tag{18}$$

where C_{BMU} and c have been defined in equation 9. Because y_0 depends on C_{BMU}, then it depends on osteocytes; therefore, the BMU integration will control the bone mass. Equation 8d is completed with y_1 and y_2, which considers the net effect on the bone mass due to osteoclasts and osteoblasts, respectively. Hence, the equation for those values is given by

$$2y_i = (s_i - \overline{s_i}) + |(s_i - \overline{s_i})|, \tag{19}$$

where it is valid for $i = 1, 2$. Depending on the type of model chosen for osteoclasts/osteoblasts, the steady state value $\overline{s_i}$ can be chosen from Table 1, equation 15, or equation 17. Thus, the deposition/resorption depends on the difference between the value of osteoblasts/osteoclasts and the steady state, which is the physiological value.

3 Computational model

The computational implementation of this model is evaluated by applying it to a benchmark problem established in prior studies [12, 13, 32, 33]. We concisely describe the computational procedure, including geometry, boundary conditions, initial conditions, and parameter overview.

3.1 Computational Procedure

Figure 2 depicts the model's algorithm, split into mechanics and biology sections. Ordinary differential equations govern osteocytes, osteoclasts, osteoblasts, and bone mass evolution within each element over time. It is important to note that there are 1000 initial days during which the temporal evolution of the cells in each element starts randomly. This randomness prevents all cells from being temporally synchronized. In the bone remodeling process, some cells will be in different remodeling phases than others, which helps maintain bone integrity. Therefore, the extended BMUs are initiated at various times (randomly) before day 1000, preventing the entire bone from oscillating synchronously. Instead, different parts of the bone undergo remodeling at different times throughout the domain. When $t = 1000$ is reached, all BMUs in every domain element are active. Although the cycle of each BMU is desynchronized with most other BMUs in the domain, the analysis of BMUs with mechanical loads and the bone damage repair process begins at this point. Therefore, $t = 1000$ serves as $t = 0$ for the model analysis. For $t < 1000$, only Komarova's model runs in each element, with temporal phase shifts in the bone remodeling cycle.. Mechanics start as BMUs enter the bone remodeling cycle, with osteocytes as damage and energy sensors. Parameters like C_{BMU} and x_0 sustain BMUs based on mechanical energy, while microdamage is monitored and repaired during cycles. Updated mechanical properties establish the constitutive relationship at each step, usually one day. BMU activation spans 1000 days across the mesh, with event calculations extending over 5000 days (total simulation of 6000 days), initiated once all finite elements have active BMUs. The mechanics model was resolved by employing finite element methods, utilizing the precision of bilinear quadrilateral elements. The ordinary differential equations were addressed within each element using a 4th-order Runge-Kutta method. At every step of the computation, where the time increment is set to $\Delta t = 1$ day, the algorithm calculates the evolution of each cell within the extended BMUs. Furthermore, it is ensured that each time step reaches the fixed point of the nonlinear problem using the Newton-Raphson method. Once the computation is complete, the algorithm seamlessly updates the mechanical properties and handles the momentum equation adeptly. To ensure the accuracy of the simulation, previous numerical studies were conducted to determine the optimal value of Δt, as explored in the comprehensive work by Ramtani et al. (2023) [24]. Additionally, careful attention was given to selecting the appropriate element size, with a refined choice of $h = 2$ mm, as elucidated in the research conducted by Garzon et al. (2012) [13].

3.2 Geometry and boundary conditions

Figure 3 showcases the geometry and boundary conditions employed to examine the strengths and weaknesses of the aforementioned model and algorithm. This benchmark model has been extensively employed in prior studies [9, 12, 32, 35], serving as a foundation for solving and comparing bone remodeling models, as well as exploring their capacity to resemble tree-like structures. This investigation utilized a bilinear quadrilateral element with an average width of 0.1 m (equivalent to 10 cm), comprising 2500 elements and 2601 nodes. A triangular distributed mechanical load was applied to the upper side. In contrast, the bottom side had constraints in the $y-$ direction, except in the right corner, where a total displacement constraint was imposed. These parameters and conditions were selected to comprehensively analyze the model and algorithm's performance. To ensure diverse initial conditions and avoid synchronicity among mesh elements during the bone remodeling cycle, we carefully selected random moments before 1000 days to define each mesh element's initial conditions for osteoclasts, osteoblasts, and bone mass. At the integration start time of $t = 1000$ days, we set the osteocytes, denoted as x_0, to initiate the Bone Multicellular Unit (BMU) integration process. Notably, the initial conditions for osteocytes, osteoclasts, osteoblasts, and bone mass percentage were set to $s_0 = 1.0$ cells, $s_1 = 11.586$ cells, $s_2 = 231.7238$ cells, and $z = 95.5\%$, respectively, as reported in [13, 23, 24].

To illustrate the results and monitor cell evolution within a single finite element, we specifically selected element number $e = 2215$, which falls within the identified damage zone as depicted in Figure 3c). Additionally, at $t = 1500$ days, we introduced induced damage by setting $D(\mathbf{x}, t) = 1.0$, and we incorporated $D_b = 0.05$ into the models governing the bone remodeling cycle for both osteoclasts and osteoblasts.

By carefully defining initial conditions, tracking cell evolution in a specific element, and introducing controlled damage scenarios, we aimed to capture the intricate dynamics of bone remodeling and gain insights into the effects of induced and biological damage on the system.

3.3 Parameters

We have extracted the relevant physiological bone remodeling parameters from the notable sources [13, 19, 23, 24, 32], which are widely recognized in the field. These parameters play a crucial role in understanding and analyzing the intricate process of bone remodeling. To facilitate comprehension and provide a comprehensive overview, we have organized and presented these parameters in a convenient tabular format, as demonstrated in Table 2. This table is a reference for researchers, clinicians, and professionals engaged in studying and evaluating bone remodeling dynamics..

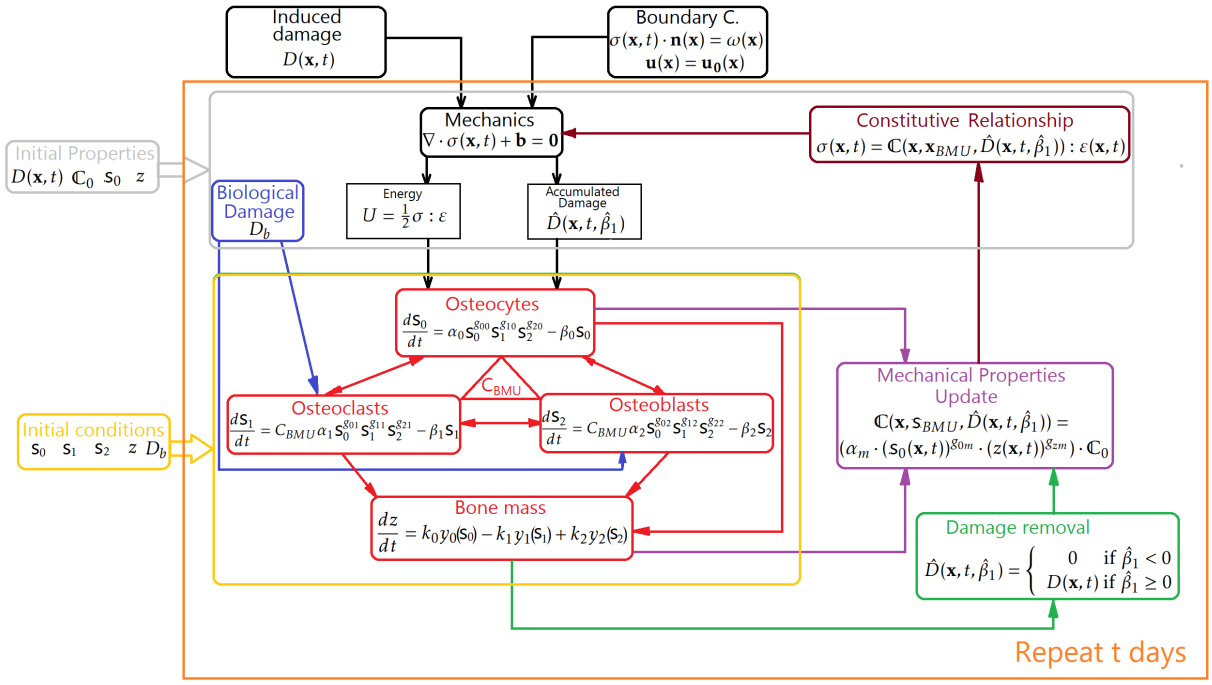

Figure 2: The algorithm starts with initial conditions for the number of cells, osteocytes, osteoclasts, and osteoblasts. Additionally, it has initial properties that change over time according to the evolution of the previously described mathematical model. The initial damage and boundary (and geometric) conditions, which remain constant for this problem, are also considered. Thus, the gray box in the figure determines the strain energy, induced biological damage, and accumulated biological damage. This data gives the evolution and response at the cellular level (osteocytes, osteoclasts, and osteoblasts) (in the yellow box). From this analysis, the evolution of bone mass and the locations of the highest cellular activity, where bone mass will be deposited to support mechanical load, are obtained. The new mechanical properties are determined with the bone mass and osteocytes, and accumulated damage is removed after reaching a maximum damage threshold to maintain proper mechanical support. Then, the entire process repeats over t days (in the orange box) for 5000 days.

3.4 Computational cases

We conducted a comprehensive analysis of the model's capabilities, utilizing the geometric configuration depicted in Figure 3. The study involved three primary simulations, each exploring distinct scenarios to assess the model's performance.

Firstly, a simulation was conducted in an undamaged domain, providing a baseline for comparison. Secondly, we introduced induced damage directly into the designated region illustrated in Figure 3c, where the damage function $D(\mathbf{x},t)$ was set to 1.0. This allowed us to evaluate the model's response to explicit mechanical damage.

In the third simulation, we incorporated biological damage into the model by introducing the term D_b into the equations governing the behavior of osteoblasts and osteoclasts. Unlike the previous scenario, mechanical damage was not directly imposed through $D(\mathbf{x},t)$. Instead, the bone remodeling process was altered by incorporating the concept of biological damage, effectively inducing damage through this mechanism.

Furthermore, the impact of biological damage was examined across different aspects of the model. Firstly, we analyzed its influence on production and removal parameters, employing equations 13. Secondly, we assessed its effect as a factor in the production term, utilizing equations 14. Lastly, we investigated the role of autocrine and paracrine factors by incorporating equations 16.

To visually represent the various cases studied in this work, Figure 4 displays the outcomes of these simulations, providing a visual summary of our findings and facilitating a comprehensive understanding of the results obtained.

4 Results and discussion

4.1 Comparison among normal and induced -or- biological damage

Figure 5 illustrates 2D visualizations of a model displaying results at t = 5000 days for a bone remodeling process without induced or external damage, i.e., physiological. The figure depicts the results for osteoclasts, osteoblasts,

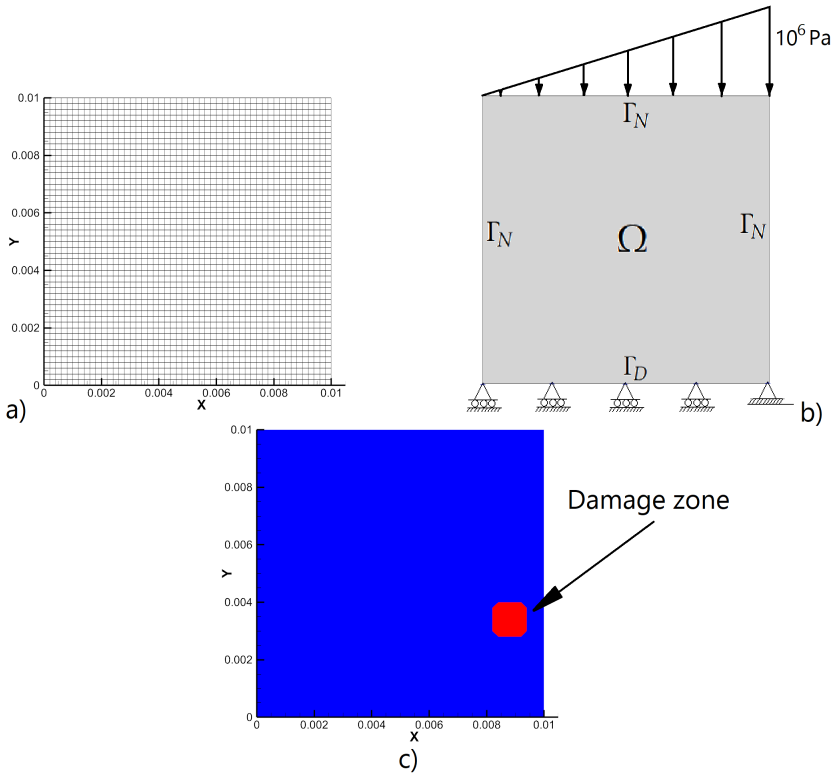

Figure 3: The square model itself has a size of 10 cm. The aforementioned details provide crucial insights into the mesh configuration, boundary conditions, and the location of the damage zone in the computational examples. a) The computational examples utilized a mesh, as depicted in Figure 3, with dimensions given in meters (m). b) The boundary conditions were imposed to ensure a benchmark example [13, 32]. The upper side of the square model, subjected to a triangular loading distribution as shown in the figure, experienced a maximum stress of 10^6 Pa. c) In the model, a specific region was designated as the damage zone. This zone encompasses 36 elements within the mesh, while the overall model consists of 2500 elements and 2601 nodes.

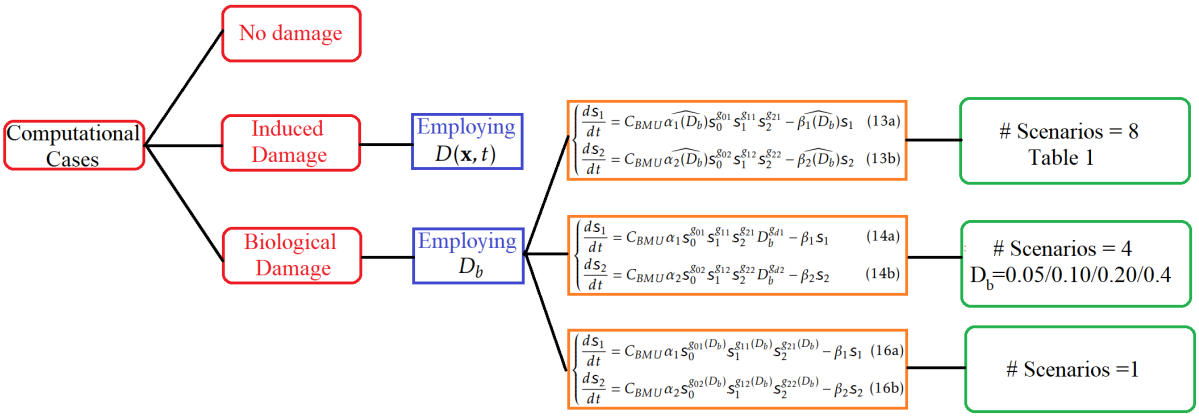

Figure 4: In this study, we examined three primary cases to investigate the effects of different damage scenarios. These cases encompassed the following: a) No Damage: This case served as a baseline. b) Induced Damage: In this case, we introduced explicit damage into the system by directly incorporating a value of $D(\mathbf{x},t) = 1.0$. c) Biological Damage: The third case explored the concept of biological damage. We investigated three distinct approaches for integrating the concept of D_b into the equations governing the behavior of osteoclasts and osteoblasts. These approaches provided different perspectives on how biological damage influences the bone remodeling process.

osteocytes, and bone mass. The figure shows how the remodeling cycle strategically reinforces bone in response

to mechanical loads, enhancing its ability to support external forces with a tree-like structure and preserving structural integrity. In previous articles, particularly in [13], one can observe two main trunks that support the triangular mechanical load applied to the structure at the top. These two main trunks extend from the top to the bottom of the geometry, with smaller branches of lower density (resembling a checkerboard pattern) that support the entire distributed load above. This structure is reminiscent of a tree supporting the weight of its fruits and branches.

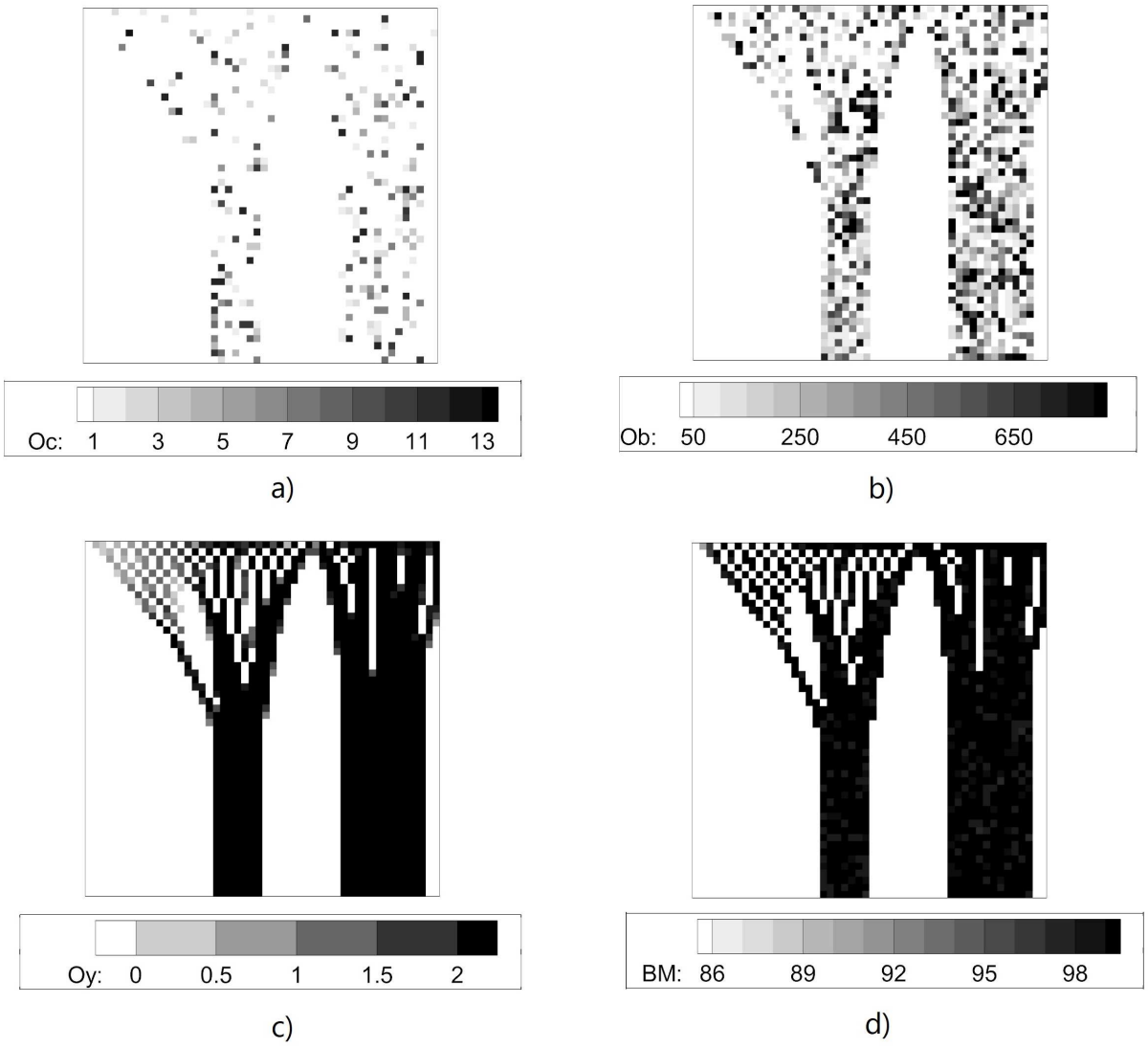

Figure 5: Results for $t = 5000$ days. The figure shows the osteoclasts (Oc), osteoblasts (Ob), osteocytes (Oy), and bone mass (BM) results. a) Osteoclasts: The figure indicates where the highest number of osteocytes is located, showing that the number is around 13 osteocytes in a finite element. b) Distribution of osteoblasts, where the maximum value is approximately 800 osteoblasts. c) Osteocytes, with a maximum value of 2.3 in a finite element. d) The distribution of bone mass is shown in percentage terms. Note the tree-like structure that has developed.

.

Figure 6 provides insights into the temporal changes in the percentage of osteoclasts, osteoblasts, osteocytes, and bone mass, considering the presence of damage. At $t = 1500$, the designated damage zone (as indicated in Figure 3c) is subjected to complete damage, where $D(\mathbf{x}_{\text{damage zone}}, t = 1500)$ is set to 1.0. The results depicted in Figure 6 demonstrate the impact of this damage on the structural integrity of the system.

Upon introducing the complete damage in the specified zone, the structure experiences a collapse, leading to the loss of elements located both above and below the damaged region. As depicted in Figure 6, this damage significantly affects the overall structure, disrupting the previously maintained tree-like configuration.

These findings highlight the vulnerability of the bone structure to damage and emphasize the crucial role of intact elements in maintaining the structural integrity necessary for load-bearing capacity. The observed conse-

quences of damage underscore the importance of understanding and addressing potential weak points to preserve the bone system's overall functionality and mechanical stability.

The analysis focuses on the evolution of various cellular components and bone mass in a 2D setting. The results are presented in Figure 6, organized into four rows representing different cell types and bone mass: the first row corresponds to osteoclasts (OC) in terms of cell count; the second row represents osteoblasts (Ob) in terms of cell count; the third row depicts osteocytes (Oy) in terms of cell count; and the fourth row shows bone mass (BM) as a percentage. The columns in Figure 6 correspond to different time points: a) The initial time. b) Time = 1700 days, illustrating the progression of the bone remodeling process in the presence of induced localized damage. c) Time = 3400 days. d) Time = 5000 days, providing insights into the later stages of the bone remodeling process under the influence of induced damage. These insights shed light on the dynamic cellular interactions and structural changes over time, contributing to our knowledge of the pathological bone remodeling process.

The previous model incorporated induced damage directly into osteocytes' behavior and mechanical properties. However, it is important to consider that factors such as tumors, necrosis, metabolic disorders, or localized abnormal cell functioning can disrupt the bone remodeling cycle. In this case (Figure 7), we introduced a localized damage zone with a value of $D_b = 0.05$ [23, 24]. This value represents the impact of the interaction between osteoclasts and osteoblasts, leading to local damage that propagates throughout the bone's tree-like structure.

At $t = 1700$ days, the propagation of the damage is still in progress, and its effects are not fully developed compared to later time points. However, even at this stage, the damage already creates a significant hole in the bone structure, which has the potential to cause collapse and weaken the overall integrity of the bone. This localized damage disrupts the harmonious coordination between osteoclasts and osteoblasts, altering the delicate balance of bone remodeling and potentially leading to detrimental consequences.

Understanding the impact of such damage on bone structure is crucial for recognizing potential vulnerabilities and addressing them in clinical settings. By studying the propagation and effects of localized damage, we can gain valuable insights into the mechanisms of bone deterioration and develop strategies to mitigate its negative effects. This will ultimately enhance the prognosis and treatment options for individuals affected by bone pathologies.

When examining the behavior of the bone remodeling cycle in the context of different scenarios, focusing on the element marked as $e = 2215$ within the damage zone provides valuable insights. Figure 8 presents the results of this analysis.

In the case of the physiological behavior depicted in blue, osteoclasts and osteoblasts maintain a consistent pattern over time, with peak and bottom values remaining stable. This indicates a well-regulated physiological cycle. This element's bone mass density (represented by the blue line as a percentage) oscillates between 87.5% and 100%, reflecting an optimal density that effectively supports external mechanical loads. Additionally, the damage experienced by this element remains within a small range (less than 20%), demonstrating that it does not significantly affect the overall structural integrity. Moreover, the damage is constantly removed throughout the process, ensuring the maintenance of a healthy bone structure.

In stark contrast, the induced damage, illustrated by the steep orange line, rapidly disrupts the bone remodeling cycle, leading to a sharp increase in damage and forming a complete damaged zone. Consequently, osteoclasts and osteoblasts lose their functionality, destroying the basic multicellular unit (BMU) and causing a dramatic reduction in bone mass.

The behavior represented by the black line in the figure corresponds to the bone remodeling cycle with biological damage, as described in Equation 16. In work by Ayati et al. [4], autocrine/paracrine factors were used to incorporate the influence of damage into the equation, specifically simulating the impact of tumors on the remodeling process. In this scenario, the abnormal bone remodeling cycle causes a significant increase in both osteoblasts and osteoclasts, leading to a peak in bone mass density followed by a rapid decline toward zero. As the bone mass approaches zero, the damage percentage reaches its maximum value of 100%. Consequently, localized damage occurs due to an abnormal bone remodeling cycle induced by external factors, such as tumors.

The three models presented in this section resemble the intricate nature of physiological bone, which continually engages in the vital process of bone regeneration. This process ensures the sustained renewal of the bone's structural integrity and the efficient removal of microdamage caused by external loads and the ongoing cellular exchange. However, in situations where damage is induced, such as during surgical interventions or instances of localized stress peaks, the resulting damage extends beyond the confines of the mechanical framework and permeates the biological aspect, as previously reported [25]. In contrast, diseases such as tumors and metastasis [17, 36] can profoundly impact the remodeling cycle, causing damage that propagates throughout the bone, thereby modifying the optimal structural characteristics observed in physiological conditions. Thus, the proposed model uniquely simulates damage in both directions accurately: from mechanical events to the biological framework and, conversely, from the biological realm to the mechanical one, capturing the dynamic interplay between these vital components.

In summary, the analysis reveals that induced mechanical damage can significantly affect the bone remodeling cycle, leading to disruptions in the physiological process and subsequent structural consequences. In contrast, biological damage can affect the mechanical integrity of the bone due to BMU damage.

4.2 Results including biological damage in Equation 13 / eight scenarios

A novel approach has been employed to capture the impact of biological damage, leading to a reevaluation of the rewriting terms α (rate of proliferation) and β (rate of removal) as was introduced in [23, 24]. These terms, which were previously considered constants, now undergo a transformation based on introducing a new variable termed D_b, representing the extent of biological damage. By utilizing functions $\alpha(D_b)$ and $\beta(D_b)$ (Table 1), the model enables the possibility of both increased and decreased rates. Specifically, when the new function multiplies the previous constant value by $\frac{1}{1-D_b}$, the rates can increase, whereas multiplying them by the factor $1 - D_b$ yields a decrease in rates. To explore the influence of biological damage, D_b is assigned values ranging from 0 to 1, and for our purposes, a specific value of $D_b = 0.05$ was chosen. Consequently, the resulting scenarios entail a combination of constant terms dynamically modified according to the value of D_b. Importantly, including additional autocrine or paracrine parameters is deemed unnecessary, as these factors have already been integrated into models two and three.

4.2.1 Scenarios 2, 3, 5, and 6

Figure 9 comprehensively depicts the results obtained when incorporating the production/removal terms to account for biological damage. Unlike the previous graphs, this figure adopts a more organized layout. The first row corresponds to osteoclasts; the second represents osteoblasts, the third depicts osteocytes, and the fourth showcases bone mass. The figure specifically focuses on the final time step $t = 6000$ days, presenting the outcomes for scenarios: a) 2, b) 3, c) 5, and d) 6.

By observing the last row of the figure, it becomes evident that the extent of biological damage differs across scenarios. Scenario 2 shows a osteocyte reduction while maintaining the bone mass percentage below the optimal level (93%). However, the damage has permeated the entire structure, indicating damage propagation. Scenarios 3, 5, and 6 exhibit similar patterns with varying degrees of propagated damage. Nonetheless, a slight excess of osteoclasts leads to a moderate mass loss, affecting the overall structure. This particular scenario may mirror an abnormal bone metabolism or an aging process, as described in detail by Armas et al. (2012) [3].

Figure 10 provides a comprehensive overview of the outcomes observed in Scenarios 2, 3, 5, and 6. Scenarios 2, 3, and 6 notably exhibit fascinating patterns characterized by damped oscillations of osteoblasts and osteoclasts, ultimately converging to distinct nontrivial steady states. In Scenario 2 (represented by the black line), the production and removal of osteoclasts are governed by the terms $\alpha_1(1 - D_b)$ and $\beta_1(1 - D_b)$, respectively. Both production and removal rates gradually decline. Conversely, we observe an increase in production and removal rates for osteoblasts. Although the results shown here cannot be validated with experimental or clinical information, it is known that in certain tumors like multiple myeloma, reduced bone mass can be attributed to decreased bone cell formation [16, 30]. Similarly, the localized damage shown here (from possible biological damage) can lead to bone damage.

Additionally, our results indicate a reduction in the bone remodeling period for osteoclasts and osteoblasts, mirroring the findings by Ayati et al. [4]. However, the system demonstrates its remarkable ability to spontaneously recover and restore its normal functionality. Approximately after $t = 4800$ days, the system undergoes a transformative phase, generating new bone mass and effectively mitigating the extent of the damage. This restorative phenomenon becomes evident in the damage graph, which initially exhibits a peak closely approaching total damage. However, as the Bone Modeling Unit (BMU) reactivates its cycle, the damage is gradually resolved, exemplifying the system's intrinsic capacity for self-repair and the resumption of its essential physiological processes.

In Scenario 3 (represented by the blue lines), the production and removal of osteoclasts are governed by the terms $\frac{\alpha_1}{1-D}$ and $\beta_1(1 - D)$, respectively. This results in an increased production of osteoclasts and a decreased removal rate, influenced by the presence of D_b. On the other hand, for osteoblasts, the terms $\alpha_2(1 - D)$ and $\frac{\beta_2}{1-D}$ lead to a decline in production and an increase in removal rates. As time progresses, the graphs representing osteoclasts and osteoblasts demonstrate a converging trend.

Upon analyzing the results depicted in Figure 10 for Scenario 3, we observe a temporary, slight decline in bone mass, followed by a substantial reduction until it reaches zero. The graph illustrating the damage progression indicates a rapid and relentless advancement towards total damage before reaching the $t = 3200$ days mark. In contrast, Scenario 6 experiences a delayed onset of damage while exhibiting similar behavior to that observed in Scenario 3. These scenarios can be likened to cases involving tumors or metastasis, characterized by distinct metabolic conditions that yield varying degrees of disease aggressiveness [23].

4.2.2 Scenarios 1, 4, 7, and 8

Figure 11 visualizes the outcomes of incorporating production/removal terms to model biological damage. It features a well-structured layout with rows dedicated to osteoclasts, osteoblasts, osteocytes, and bone mass. The focus is on the final time step of $t = 6000$ days, showcasing the results for scenarios a) 1, b) 4, c) 7, and d) 8.

Scenarios 1 and 8 demonstrate a noticeable trend in which the bone mass is maintained over time but with deteriorated characteristics. This is primarily caused by the decline in osteoblasts and osteoclasts, resulting in a loss of Bone Modeling Units (BMUs) and a disruption in the bone remodeling process. Consequently, there is an

accumulation of microdamage over time, leading to a gradual deterioration of the mechanical properties in that area and causing mechanical damage in the tree-like bone structure.

In contrast, Scenario 7 stands out with an observed increase in bone mass. Although there is no direct correspondence with clinical or experimental evidence, it can be compared to the patterns observed in osteoblastic tumors. These tumors typically exhibit excessive production of osteoblasts, leading to abnormal bone growth and an overall increase in bone mass [20]. These tumors typically exhibit an excessive production of osteoblasts, which leads to abnormal bone growth and an overall increase in bone mass.

The divergent outcomes displayed by these scenarios highlight the significance of various factors in bone health and remodeling. While Scenarios 1 and 8 indicate the detrimental consequences of disrupted BMUs, Scenario 5 showcases the potential impact of specific pathological conditions such as osteoblastic tumors.

Figure 11 showcases Scenarios 1, 4, 7, and 8 outcomes at element $e = 2225$. In Scenario 1, the graphs reveal an initial oscillatory response characterized by a rise in BMU cells. However, this oscillation gradually diminishes, leading the system to converge towards zero for osteoclasts and osteoblasts. The bone mass density reaches a stable value of 102%, exhibiting no further oscillations over time. This behavior bears a resemblance to certain non-tumor or non-cancer-related diseases. One such example is Legg-Calve-Perthes disease, commonly observed in children, where the bone experiences reduced blood supply, resulting in a deficiency of bone precursor cells. Consequently, the bone tissue cannot undergo proper renewal, and repeated mechanical loads lead to the accumulation of fractures, ultimately causing mechanical collapse.

Examining Figure 12, Scenarios 4 and 8, akin to Scenario 1, also demonstrate a loss of oscillation over time. However, a notable difference arises: these scenarios exhibit an additional cycle of oscillation, with the period of the cycle increasing as time progresses. In contrast, Scenario 7 displays an intriguing pattern of increasing bone mass. This can be attributed to a slight decrease in osteoclasts compared to osteoblasts, resembling the characteristics of osteoblastic tumors [20].

4.3 Results including biological damage in Equation 14 / four scenarios

Figure 13 presents the results for the second model investigated in this study, offering valuable insights into the behavior of the tree-like structure under different scenarios. Scenarios with $D_b = 0.05$, 0.10, and 0.20 demonstrate comparable outcomes in a two-dimensional setting, where the tree-like structure is progressively lost. This implies that the presence of damage leads to a deterioration of the structural integrity, irrespective of the specific damage level. However, it is Scenario $D_b = 0.40$ that stands out, exhibiting a remarkable and rapid increase in bone mass. Such a pattern could indicate a tumor localized within the damaged zone, exerting a significant impact on the bone remodeling dynamics.

Turning our attention to Figure 14, we gain a more comprehensive understanding of the temporal evolution of osteoclasts, osteoblasts, bone mass, and damage. These dynamic graphs provide valuable insights into how the various components interact and change over time, shedding light on the underlying processes and their intricate interplay.

5 Conclusion

This study introduces a novel framework for modeling the bone remodeling process, offering valuable insights into the intricate interplay between biological events and mechanical dynamics. While the current model does not explicitly incorporate a multiscale approach, it leverages the computation of Bone Modeling Unit (BMU) components over time, simulating a multiscale-like model that captures both the biological and mechanical aspects of bone remodeling. Comparisons can be drawn between the 2D model and previous studies conducted by [13, 32, 33], where the formation of a tree-like structure was observed. However, this new framework goes beyond structural formation and delves into the simultaneous progression of biological and mechanical events.

One noteworthy aspect of this model is its ability to reproduce the temporal evolution of damage and the subsequent renewal of bone in each remodeling cycle. This represents a significant advancement, as it provides insights into how damage accumulates over time and how bone regeneration occurs in response. By including damage as an integral component, this model uncovers the complex bidirectional relationship between biological events and mechanical properties. The presence of induced damage can influence biological processes, while biological damage, in turn, can impact the structure and mechanical characteristics of the bone.

Furthermore, this framework can be extended to incorporate various diseases such as tumors, necrosis, abnormal metabolic events, or the aging process. By introducing a parameter that accounts for these diseases, the model can generate bone mass distributions consistent with the expected patterns observed in affected individuals. This capability represents a significant departure from previous works, as it enables the "in silico" reproduction of different pathological conditions in bone and provides insights into their interplay with mechanical dynamics.

For instance, extensive research has been devoted to developing mathematical models for predicting and studying tumor and cancer progression. Several studies [2, 8, 18, 21, 29] have aimed to establish various scenarios that shed light on the effects of biological and induced damage on bone tissue. Experimental and clinical investigations have consistently observed a gradual increase in osteoclasts over time, often accompanied by a reduction in

osteoblast production [22, 36]. This imbalance between formation and resorption gives rise to osteolysis, a key aspect of pathogenesis in conditions like myeloma [22]. Multiple myeloma is associated with elevated blood calcium levels and fractures and complications such as anemia, hypercalcemia, and renal insufficiency [36].

Researchers have explored the role of bone tissue as a tumor microenvironment, recognizing its significance in the metastatic process [17]. Metastasis in bone can be categorized as osteolytic, characterized by excessive resorption resulting from an imbalance caused by heightened osteoclast activity or reduced bone remodeling [10, 17]. This form of metastasis is commonly observed in lung and breast cancer. Conversely, an imbalance favoring bone formation leads to osteoblastic (osteosclerotic) metastasis [10, 17], which is more prevalent in prostate cancer and certain pathological conditions involving abnormal bone formation. The models described in this study aim to capture the intricate dynamics and interplay between the bone remodeling process and tumor growth. Moreover, they serve as valuable tools for exploring diverse scenarios and types of tumors, empowering researchers to propose and test treatments in a simulated environment and forecast the effects of tumors on the remodeling process over time.

These models offer the potential to manipulate the remodeling cycle by promoting differentiation, adjusting the frequency of remodeling, or modulating the deposition of bone mass within a controlled mathematical laboratory setting. This provides a platform for investigating alternative strategies and interventions to mitigate the impact of tumors on bone tissue. Ultimately, these mathematical models contribute to advancing our understanding of the complex relationship between tumor growth and the bone remodeling process, facilitating the acquisition of invaluable knowledge in the field.

While this research provides valuable insights for the academic community dedicated to bone disease research, it is important to acknowledge certain limitations that should be addressed in future studies. Firstly, the model employed in this work is based on Komarova's model [19], which represents an abstraction of reality. The parameters used in the model are obtained from stability analysis [23] and capture quantities such as the initial number of osteoblasts and osteoclasts, bone oscillation, and the time period for mass replacement. Komarova et al. formulated a mathematical model that aligns with experimental observations. Similarly, modifications to Komarova's seminal model have been made using parameters derived from stability analysis. However, it is crucial for future research to compare the mathematical model and its parameters with experimental evidence to validate their applicability.

It is important to note that the precise relationship between diseases and the bone remodeling process remains unknown. Future investigations should consider the effects of drugs used to improve bone mass or alter its quality. Each modification to the model should be carefully compared with real diseases, and techniques such as statistics and machine learning could be employed to identify model variations and refine the associated parameters. This iterative approach would enhance the model's ability to accurately represent the complexities of bone diseases and their impact on the bone remodeling process.

In future work, we aim to further investigate the parameters of this model through a comprehensive sensitivity analysis, delving into their individual and collective influences on the system dynamics. Additionally, we plan to extend the model to more realistic and intricate geometries, allowing for a more accurate representation of the bone remodeling process in three-dimensional (3D) settings. By expanding the model to 3D, we can capture the spatial variations and intricate interactions within the bone tissue, providing a deeper understanding of its behavior.

Furthermore, we intend to explore the model's applicability to specific diseases and pathological conditions, such as tumors, necrosis, and aging events. By examining these cases in light of the model, we can assess its capabilities and its ability to mimic the complexities observed in real pathological scenarios. This exploration will contribute to elucidating the relationship between the bone remodeling process and various diseases, ultimately aiding in the development of targeted interventions and treatment strategies.

Through these future endeavors, we seek to enhance the model's accuracy, expand its scope, and uncover valuable insights into the intricate interplay between bone remodeling and pathological conditions. By refining the model and exploring its capabilities in different contexts, we hope to advance our understanding of bone diseases and contribute to the development of innovative therapeutic approaches.

In summary, this new framework presents a promising avenue for studying bone remodeling processes by integrating biological and mechanical events. Its ability to simulate diseases and investigate their impact on bone structure and mechanics opens up new possibilities for understanding the underlying mechanisms and developing potential interventions.

6 Declarations

6.1 Ethical Approval

This declaration is not applicable.

6.2 Competing interests

All authors declare no competing or finantial interest.

6.3 Authors' contributions

All author contributed to every stage of the research of this paper from conceptualization, through methodology, investigation, formal analysis, writing, editing, software reviewing and supervision.

6.4 Funding

This work was supported by Biotechnology Institute - Universidad Nacional de Colombia, Laboratoire CSPBAT, equipe LBPS, CNRS (UMR 7244),Universit e Sorbonne Paris Nord and Department of Mechanical Engineering,.

6.5 Availability of data and materials

The data obatined on the solution of these models can be accessed by sending an email to the corresponding author.

References

[1] I. Ait Oumghar, A. Barkaoui, T. Merzouki, D. Guenoun, and P. Chabrand. Chemotherapy and adjuvant therapies' impact on the internal remodeling process of bone and its mechanical behavior for breast cancer patients. *International Journal for Numerical Methods in Biomedical Engineering*, 40(1):e3788, Jan 2024. doi: 10.1002/cnm.3788.

[2] Philipp M Altrock, Lin L Liu, and Franziska Michor. The mathematics of cancer: integrating quantitative models. *Nature Reviews Cancer*, 15(12):730–745, 2015.

[3] L.A. Armas and R.R. Recker. Pathophysiology of osteoporosis: new mechanistic insights. *Endocrinol Metab Clin North Am.*, 41(3):475–86., 2012.

[4] Bruce P Ayati, Claire M Edwards, Glenn F Webb, and John P Wikswo. A mathematical model of bone remodeling dynamics for normal bone cell populations and myeloma bone disease. *Biology direct*, 5(1):1–17, 2010.

[5] Marcelo Tavares Bahia, Mariana Barros Hecke, Eleonora Gouveia Farias Mercuri, and Marcelo Martins Pinheiro. A bone remodeling model governed by cellular micromechanics and physiologically based pharmacokinetics. *Journal of the Mechanical Behavior of Biomedical Materials*, 104:103657, Apr 2020. doi: 10.1016/j.jmbbm.2020.103657.

[6] J. Baldonedo, J. R. Fernández, and A. Segade. Analysis of a bone remodeling model with myeloma disease arising in cellular dynamics. *International Journal for Numerical Methods in Biomedical Engineering*, 36(6): e3333, Jun 2020. doi: 10.1002/cnm.3333.

[7] N. Bonfoh, E. Novinyo, and P. Lipinski. Modeling of bone adaptive behavior based on cells activities. *Biomechanics and Modeling in Mechanobiology*, 10(5):789–798, Oct 2011. doi: 10.1007/s10237-010-0274-y.

[8] Dana-Adriana Botesteanu, Stanley Lipkowitz, Jung-Min Lee, and Doron Levy. Mathematical models of breast and ovarian cancers. *Wiley Interdisciplinary Reviews: Systems Biology and Medicine*, 8(4):337–362, 2016.

[9] G. Chen, G. Pettet, M. Pearcy, and D. L. S. McElwain. Comparison of two numerical approaches for bone remodelling. *Medical Engineering & Physics*, 29(1):134–139, 2007.

[10] Robert E Coleman. Clinical features of metastatic bone disease and risk of skeletal morbidity. *Clinical cancer research*, 12(20):6243s–6249s, 2006.

[11] C.V. Cook, A.M. Lighty, B.J. Smith, and A.N. Ford Versypt. A review of mathematical modeling of bone remodeling from a systems biology perspective. *ChemRxiv*, Preprint(doi:10.26434/chemrxiv-2024-5vrcc), 2024.

[12] D. P. Fyhrie and M. B. Schaffler. The adaptation of bone apparent density to applied load. *Journal of Biomechanics*, 28(2):135–146, 1995.

[13] D. A. Garzón-Alvarado and D. Linero. Comparative analysis of numerical integration schemes of density equation for a computational model of bone remodelling. *Computer Methods in Biomechanics and Biomedical Engineering*, 15(11):1189–1196, 2012.

[14] Ridha Hambli. Connecting mechanics and bone cell activities in the bone remodeling process: an integrated finite element modeling. *Frontiers in Bioengineering and Biotechnology*, 2:6, Apr 2014. doi: 10.3389/fbioe.2014.00006.

[15] Ridha Hambli, Mohamed Hédi Boughattas, Jean-Luc Daniel, and Azeddine Kourta. Prediction of denosumab effects on bone remodeling: A combined pharmacokinetics and finite element modeling. *Journal of the Mechanical Behavior of Biomedical Materials*, 60:492–504, Jul 2016. doi: 10.1016/j.jmbbm.2016.03.010.

[16] Douglas E Joshua, Christian Bryant, Caroline Dix, John Gibson, and Joy Ho. Biology and therapy of multiple myeloma. *Medical Journal of Australia*, 210(8):375–380, 2019.

[17] Tiina E Kähkönen, Jussi M Halleen, and Jenni Bernoulli. Osteoimmuno-oncology: Therapeutic opportunities for targeting immune cells in bone metastasis. *Cells*, 10(6):1529, 2021.

[18] Marek Kimmel. Evolution and cancer: a mathematical biology approach, 2010.

[19] Svetlana V Komarova, Robert J Smith, S Jeffrey Dixon, Stephen M Sims, and Lindi M Wahl. Mathematical model predicts a critical role for osteoclast autocrine regulation in the control of bone remodeling. *Bone*, 33 (2):206–215, 2003.

[20] S.C. Lin, L.Y. Yu-Lee, and S.H. Lin. Osteoblastic factors in prostate cancer bone metastasis. *Curr Osteoporos Rep.*, 16(6):642–647, 2018.

[21] Miguel Angel Medina. Mathematical modeling of cancer metabolism. *Critical reviews in oncology/hematology*, 124:37–40, 2018.

[22] Cristina Panaroni, Andrew J Yee, and Noopur S Raje. Myeloma and bone disease. *Current osteoporosis reports*, 15(5):483–498, 2017.

[23] S. Ramtani, J.F. Sánchez, A. Boucetta, R. Kraft, J.J. Vaca-González, and D.A. Garzón-Alvarado. A coupled mathematical model between bone remodeling and tumors: a study of different scenarios using komarova's model. *Biomech Model Mechanobiol*, 2023.

[24] S. Ramtani, L. Toudji, A. Boucetta, T. Boukharouba, and D.A. Garzón-Alvarado. Komarova's bone remodeling type model revisited within the context of a new parameter affecting both production and removal activities of osteoblasts and osteoclasts. *Journal of Mechanics in Medicine and Biology*, 2023.

[25] H. Razi, J. Predan, F.D. Fischer, O. Kolednik, and Fratzl P. Damage tolerance of lamellar bone. *Bone*, 130: 115102, 2020.

[26] Marc D. Ryser, Svetlana V. Komarova, and Nilima Nigam. The cellular dynamics of bone remodeling: A mathematical model. *SIAM Journal on Applied Mathematics*, 70(6):1899–1921, 2010.

[27] M.D. Ryser, N. Nigam, and S.V. Komarova. Mathematical modeling of spatio-temporal dynamics of a single bone multicellular unit. *J Bone Miner Res.*, 24(5):860–870, 2009.

[28] M.D. Ryser, Y. Qu, and S.V. Komarova. Osteoprotegerin in bone metastases: Mathematical solution to the puzzle. *PLoS Comput Biol*, 8(10)(e1002703), 2012.

[29] Alex Simmons, Pamela M Burrage, Dan V Nicolau Jr, Sunil R Lakhani, and Kevin Burrage. Environmental factors in breast cancer invasion: a mathematical modelling review. *Pathology*, 49(2):172–180, 2017.

[30] Cheng-Xian Song, Sheng-Yao Liu, Wen-Ting Zhu, Shao-Yong Xu, and Guo-Xin Ni. Excessive mechanical stretch-mediated osteoblasts promote the catabolism and apoptosis of chondrocytes via the wnt/β-catenin signaling pathway. *Molecular Medicine Reports*, 24(2):1–10, 2021.

[31] A. S. K. Verbruggen and L. M. McNamara. Mechanoregulation may drive osteolysis during bone metastasis: A finite element analysis of the mechanical environment within bone tissue during bone metastasis and osteolytic resorption. *Journal of the Mechanical Behavior of Biomedical Materials*, 138:105662, Feb 2023. doi: 10.1016/j.jmbbm.2023.105662.

[32] H. Weinans, R. Huiskes, and H.J. Grootenboer. The behavior of adaptive bone-remodeling: Simulation models. *J. Biomechanics*, 25(12):1425–1441, 1992.

[33] H. Weinans, R. Huiskes, and H.J. Grootenboer. Effects of fit and bonding characteristics of femoral stems on adaptive bone remodeling. *J. Biomechanical Engineering*, 116:393–400, 1994.

[34] P. Wriggers. "contact kinematics". *in Computational Contact Mechanics, Springer Berlin.*, chapter 4:56–67, 2006.

[35] Z. Xinghua, G. He, Z. Dong, and G. Bingzhao. A study of the effect of non-linearities in the equation of bone remodeling. *Journal of Biomechanics*, 35(7):951–960, 2002.

[36] Peipei Yang, Ying Qu, Mengyao Wang, Bingyang Chu, Wen Chen, Yuhuan Zheng, Ting Niu, and Zhiyong Qian. Pathogenesis and treatment of multiple myeloma. *MedComm*, 3(2):e146, 2022.

[37] X. Yang, P. Liu, H. Xing, X. Wen, Y. Wang, C. Hu, L. Li, and W. Ma. Skull modulated strategies to intensify tumor treating fields on brain tumor: a finite element study. *Biomechanics and Modeling in Mechanobiology*, 21 (4):1133–1144, Aug 2022. doi: 10.1007/s10237-022-01580-7.

Table 2: Parameters used in this work.

Parameter	Action	Value
Mechanical Parameters		
E	Young Modulus	64 MPa [13, 32, 33]
ν	Poisson Modulus	0.3 [13, 32, 33]
U_{ref}	Reference energy	800 Pa [13, 32, 33]
g_{0m}	osteocyte-derived paracrine regulation	2 [13, 32, 33]
g_{zm}	bone mass-derived strenght material constant	0
α_{m0}	Level of damage constant	1 $\#cell^{-2}$
θ	level of damage accumulation	0.01 $MPa^{-1} \cdot days^{-1}$
r	Number of points for sensing bone mass	3
General Biological Parameters		
c	BMU integration	1.0
W	BMU energy activation	0.50
k	Osteocyte production rate	0.3125 $days^{-1}$ [13, 32, 33]
g_{00}	osteocyte autocrine regulation	1 [13, 32, 33]
g_{10}	osteoclast-derived paracrine regulation	0
g_{20}	osteoblast-derived paracrine regulation	0
f	Damage factor on osteocytes	1
d	Damage limit factor before collapse	0.4
α_1	Osteoclast production rate	3 osteoblasts .day^{-1} [19]
α_2	Osteoblast production rate	4 osteoblasts .day^{-1} [19]
β_1	Osteoclast removal rate	0.2 osteoclasts .day^{-1} [19]
β_2	Osteoblast removal rate	0.02 osteoclasts .day^{-1} [19]
g_{01}	osteocyte-derived paracrine regulation	0
g_{11}	osteoclast autocrine regulation	1.1[19]
g_{21}	osteoblast-derived paracrine regulation	-0.5[19]
g_{02}	osteocyte-derived paracrine regulation	0
g_{12}	osteoclast-derived paracrine regulation	1[19]
g_{22}	osteoblast autocrine regulation	0[19]
k_0	Normalized activities of bone formation/resorption	1.0 % osteoclasts^{-1}day^{-1}
k_1	Normalized activities of bone resorption	0.093 % osteoclasts^{-1}day^{-1}[19]
k_2	Normalized activities of bone formation	0.0008 % osteoblasts^{-1}day^{-1}[19]
D_b	Biological damage	0.05 dimensionless[used in all the models here presented, except second model tested, with 0.10,0.20,0.40] (computed)
Parameters for second model [24]		
g_{d1}	Disease-derived paracrine regulation	-0.1[23, 24]
g_{d2}	Disease-derived paracrine regulation	0[23, 24]
Parameters for second model[4]		
r_{11}	Parameter afecting osteoclast-autocrine factor	0.05 [4]
r_{21}	Parameter afecting osteoblast-paracrine factor	0.0 [4]
r_{12}	Parameter afecting osteoclast-paracrine factor	0.0 [4]
r_{22}	Parameter afecting osteoblast-autocrine factor	0.2 [4]

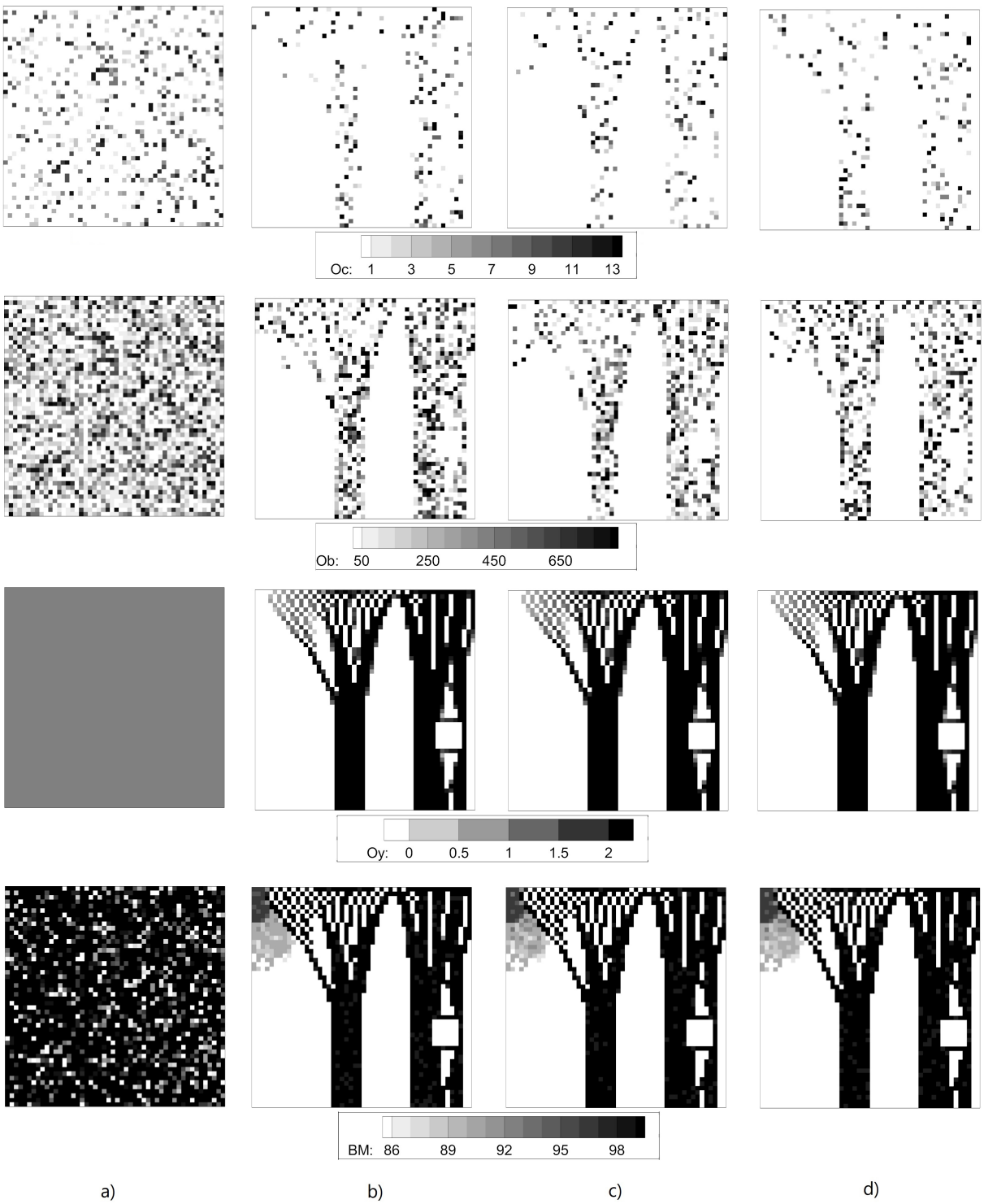

Figure 6: Results of the bone remodeling process in a pathological case with localized damage induction. The image is organized into rows (determined by cell type) and columns (determined by the evolution time, specifically columns a), b), c), and d)). The results for osteoclasts are observed in the first row (top row). The second row shows the results for osteoblasts, the third row for osteocytes, and the last row for bone mass. The columns represent different times: a) 1000 days (0 days of evolution for "all" cells in the bone), b) 2300 days, c) 3600 days, and d) 6000 days. It is important to note that there are 1000 initial days during which the temporal evolution of the cells in each element starts randomly. This randomness prevents all cells from being temporally synchronized. In the bone remodeling process, some cells will be in different remodeling phases than others, which helps maintain bone integrity. Note the original defect and how it has caused extensive damage to the bone.

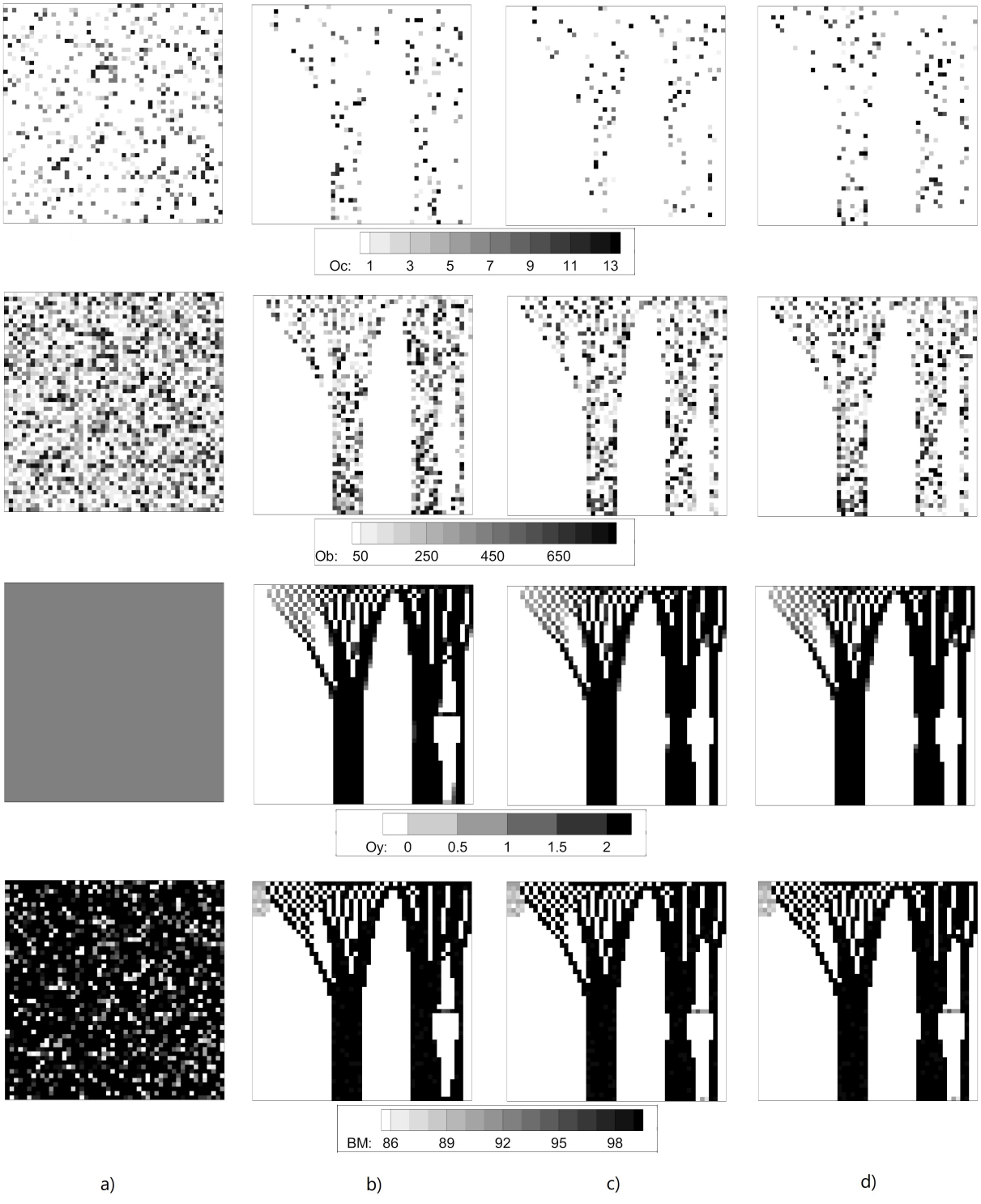

Figure 7: Results for the bone remodeling process in 2D for a pathological case when the cycle of the remodeling process is altered (see the text). It has the same conventions as before. The image is organized into rows (determined by cell type) and columns (determined by the evolution time, specifically columns a), b), c), and d)). The results for osteoclasts are observed in the first row (top row). The second row shows the results for osteoblasts, the third row for osteocytes, and the last row for bone mass. The columns represent different times: a) 1000 days (0 days of evolution for all cells in the bone), b) 2300 days, c) 3600 days, and d) 6000 days. It is important to note that there are 1000 initial days during which the temporal evolution of the cells in each element starts randomly. This randomness prevents all cells from being temporally synchronized. In the bone remodeling process, some cells will be in different remodeling phases than others, which helps maintain bone integrity. Note the original defect and how it has caused extensive damage to the bone.

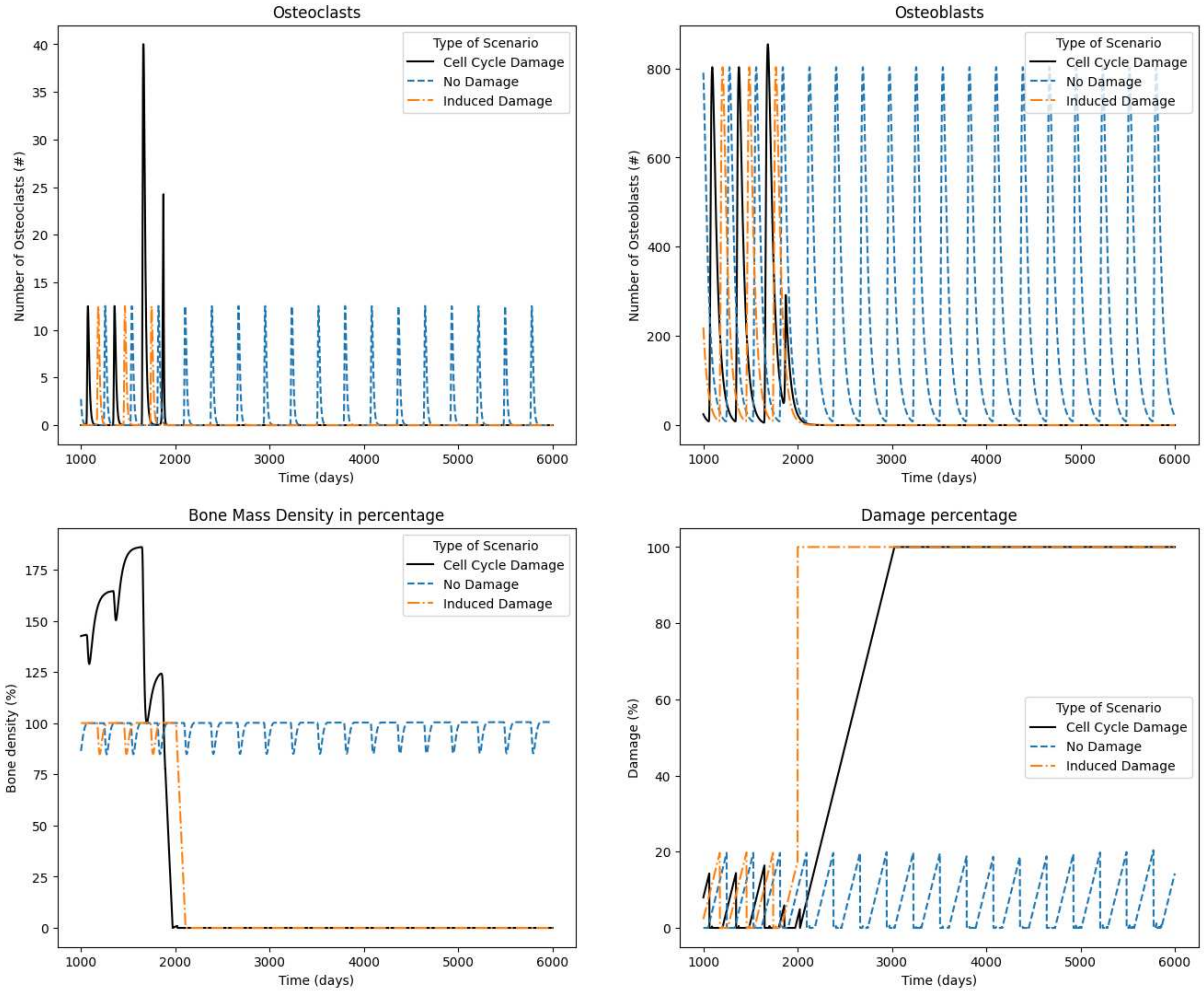

Figure 8: The graph shows the time evolution of osteoclasts (top left), osteoblasts (top right), bone mass density (bottom left), and damage (bottom right). There are three scenarios (see the color coding in the figure): Physiological (No damage), bone remodeling cycle altered (Cell cycle damage), and induced damage. These results correspond to a finite element chosen in the damaged region (see text) of Figures 5, 7, and 6, respectively.

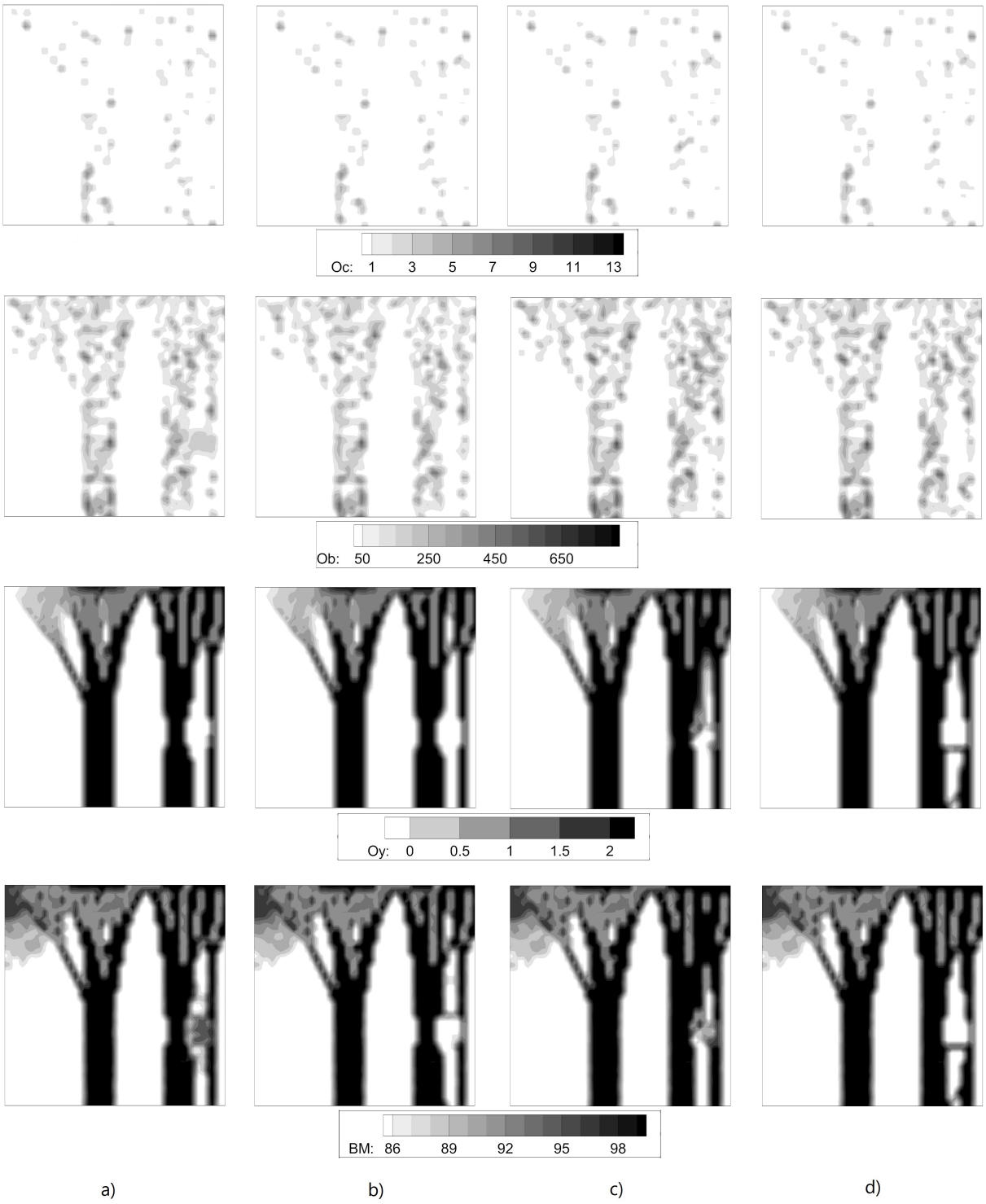

Figure 9: Results for the bone remodeling process in 2*D* for pathological scenarios 2, 3, 5 and 6 of the model in the last day of simulation (day 5000) [23, 24]. By rows (from top to bottom): first row (OC): Osteoclasts cells (in number #); second row (Ob): Osteoblasts cells (in number #); Third row (Oy): Osteocytes cells (in number #); Fourth row (BM): Bone Mass (Percentage %). By Columns: a) Scenario 2; b) Scenario 3; c) Scenario 5; and d) Scenario 6.

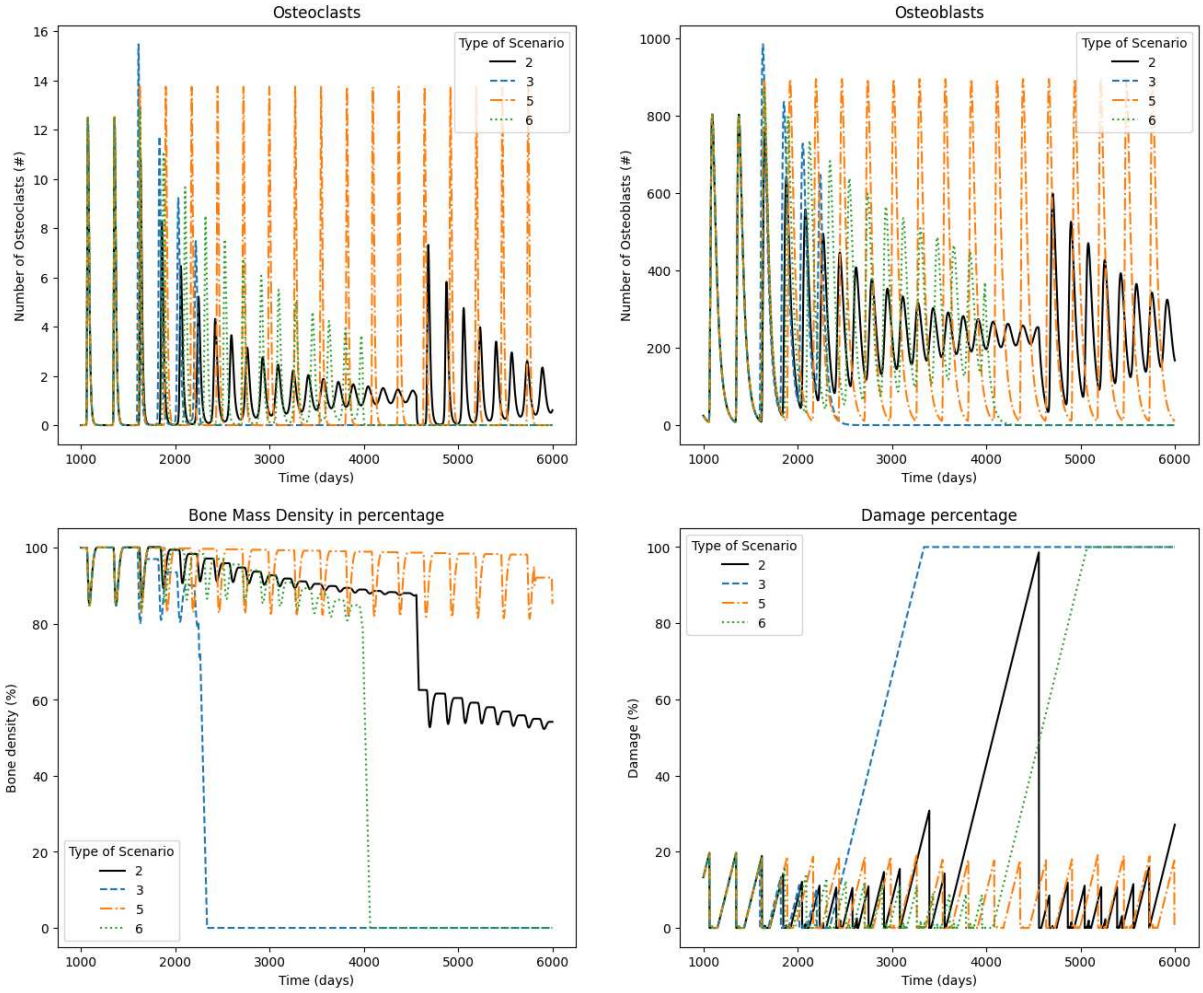

Figure 10: Results for a finite element chosen into the ”damage” region for scenarios 2, 3, 5, and 6 given in [23] and [24]. Please refer to Figure 9. The graph shows the time evolution of osteoclasts (top left), osteoblasts (top right), bone mass density (bottom left), and damage (bottom right). There are four scenarios (see the color coding in the figure and the text for the origin of each scenario).

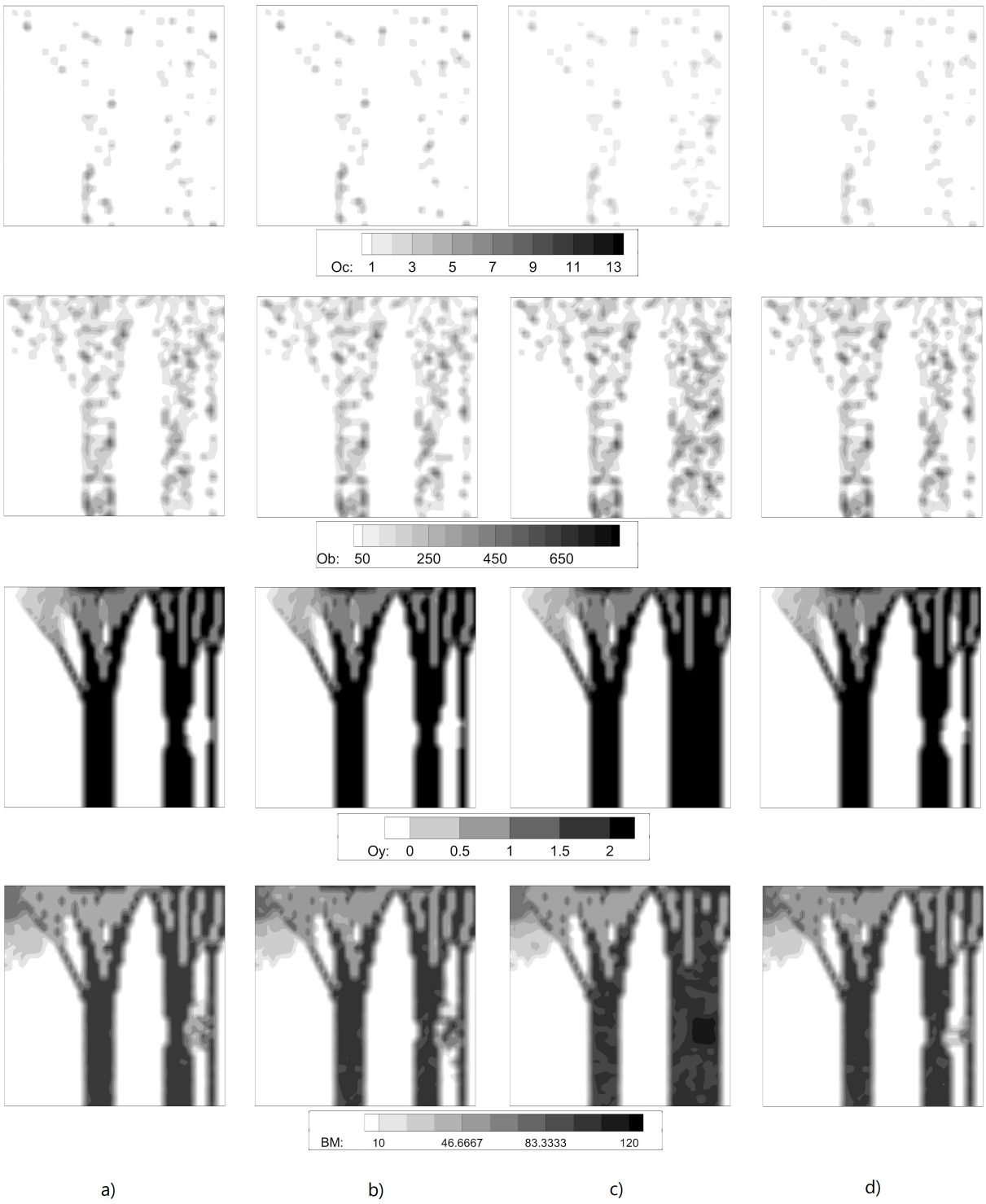

Figure 11: Results for the bone remodeling process in 2*D* for pathological scenarios 1, 4, 7, and 8 of the model in the last day of simulation (day 5000) [23, 24]. By rows (from top to bottom): first row (OC): Osteoclasts cells (in number #); second row (Ob): Osteoblasts cells (in number #); Third row (Oy): Osteocytes cells (in number #); Fourth row (BM): Bone Mass (Percentage %). By Columns: a) Scenario 1; b) Scenario 4; c) Scenario 7; and d) Scenario 8.

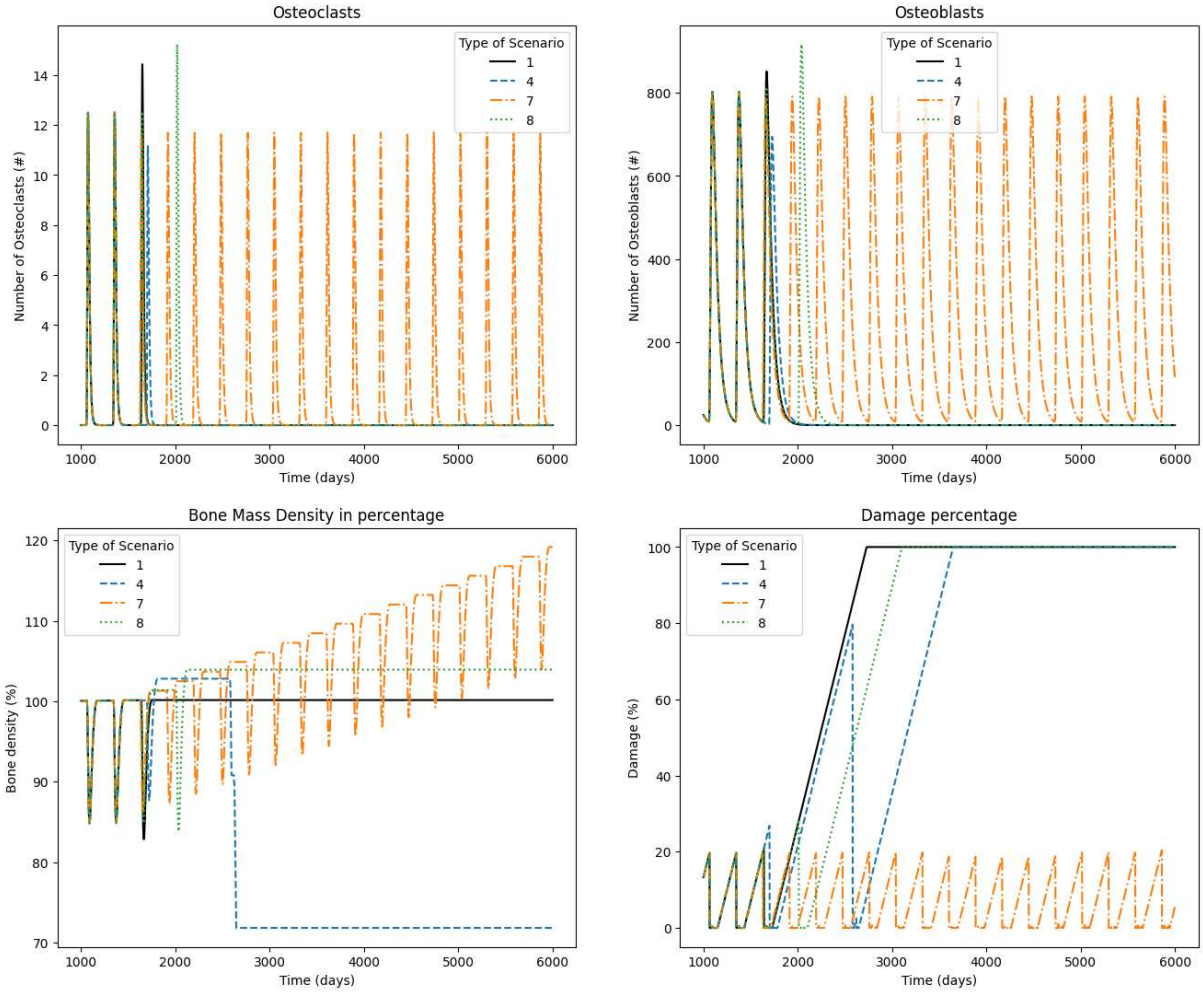

Figure 12: Results for a finite element chosen into the ”damage” region for scenarios 1, 4, 7, and 8 given in [23] and [24]. Please refer to Figure 11.The graph shows the time evolution of osteoclasts (top left), osteoblasts (top right), bone mass density (bottom left), and damage (bottom right). There are three scenarios (see the color coding in the figure).

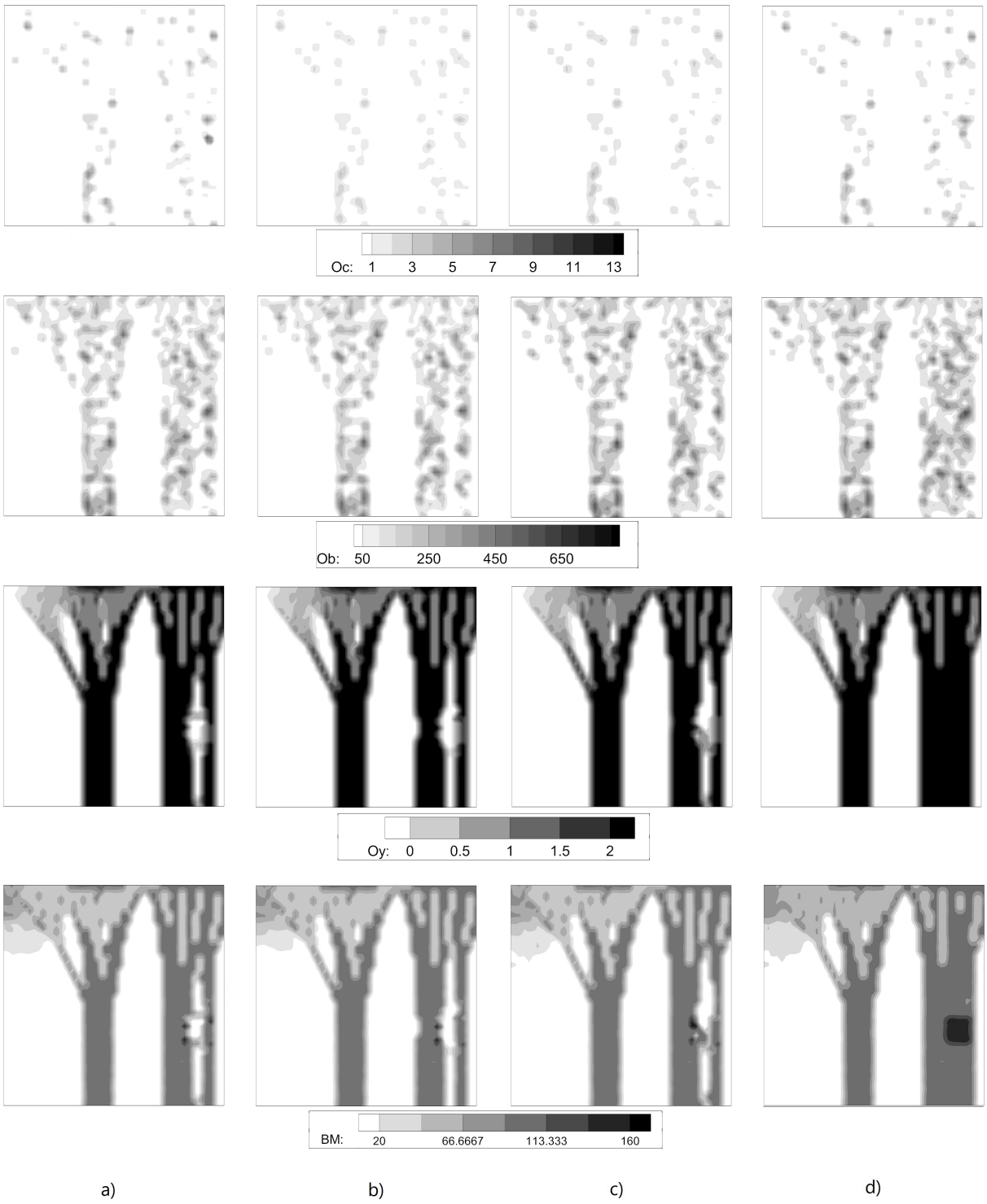

Figure 13: Results for the bone remodeling process in $2D$ for pathological scenarios by columns, a) $D_b = 0.05$, b)$D_b = 0.10$, c)$D_b = 0.20$, and d)$D_b = 0.40$ of the model in the last day of simulation (day 6000) [23, 24]. By rows (from top to bottom): first row (OC): Osteoclasts cells (in number #); second row (Ob): Osteoblasts cells (in number #); Third row (Oy): Osteocytes cells (in number #); Fourth row (BM): Bone Mass (Percentage %).

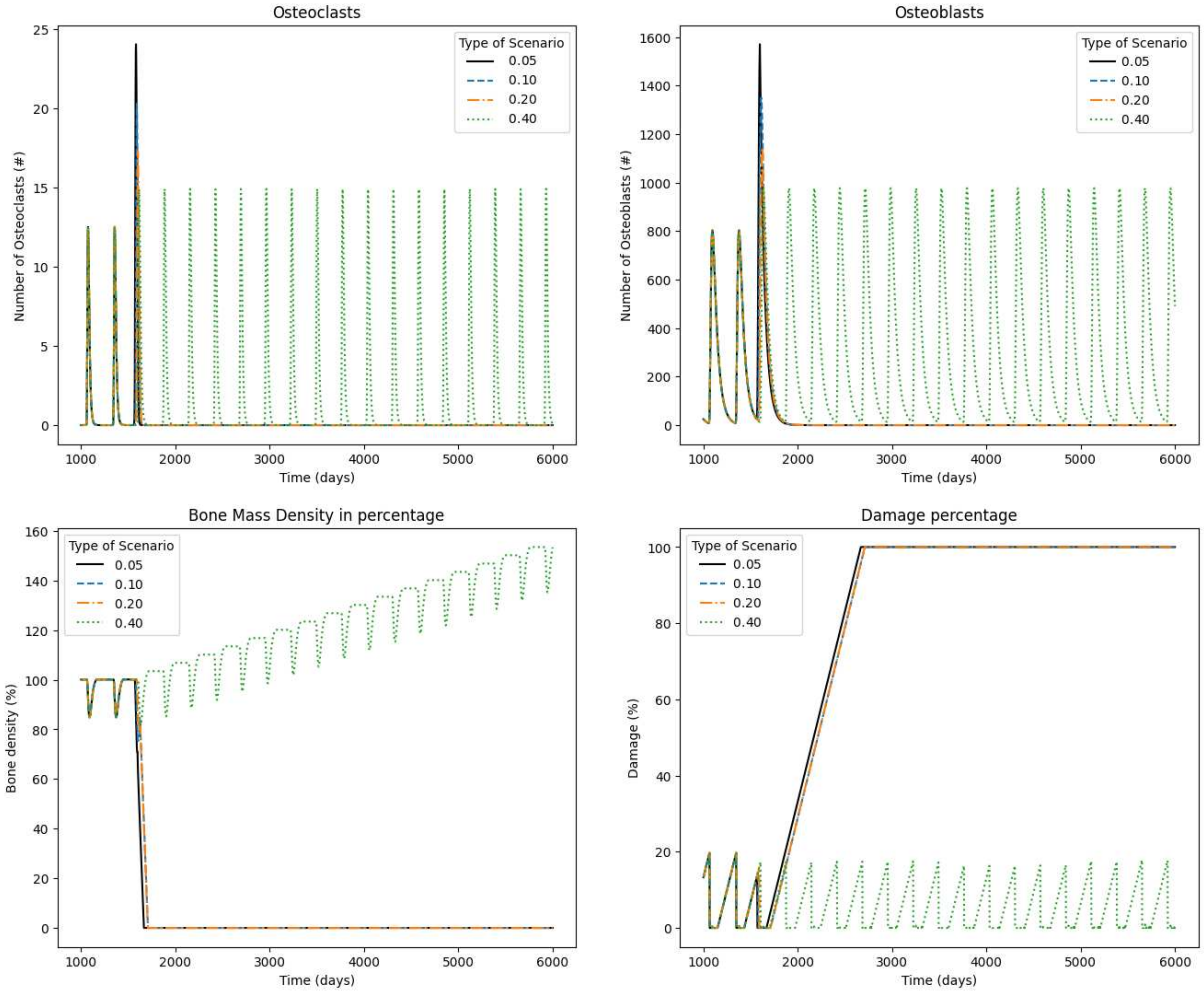

Figure 14: Results for a finite element chosen into the "damage" region for scenarios $D_b = 0.05$, $D_b = 0.10$, $D_b = 0.20$, and $D_b = 0.40$ given in [23] and [24]. Please refer to Figure 13. The graph shows the time evolution of osteoclasts (top left), osteoblasts (top right), bone mass density (bottom left), and damage (bottom right). There are three scenarios (see the color coding in the figure).